

---

# AN ALE APPROACH TO REDUCE SPURIOUS NUMERICAL MIXING THROUGH VARIATIONAL MINIMIZERS: APPLICATION TO INTERNAL WAVES

---

**Andreas Alexandris-Galanopoulos**

School of Naval Architecture and Marine Engineering  
National Technical University of Athens  
Zografos, 15710, Athens  
[andreas\\_alexandris@mail.ntua.gr](mailto:andreas_alexandris@mail.ntua.gr)

**George Papadakis**

School of Naval Architecture and Marine Engineering  
National Technical University of Athens  
Zografos, 15710, Athens  
[papis@fluid.mech.ntua.gr](mailto:papis@fluid.mech.ntua.gr)

November 26, 2025

## ABSTRACT

Spurious numerical mixing is a frequent phenomenon in ocean models. In the present paper, we present an efficient and robust methodology that defines the vertical grid motion so that this mixing is reduced. This motion is defined through the solution of an optimization problem that -using the ideas of the calculus of variations- results in an elliptic equation. This framework is generally applicable to any ocean model that uses an ALE vertical coordinate and can be tuned to fit the modeler's specific needs based on the guidelines presented herein. The method is applied to the nonhydrostatic solver presented by the authors in [1] and its applicability in fully nonlinear internal waves is investigated for the demanding test cases of wave breaking and overturning. These numerical benchmarks show the ability of the method to reduce spurious mixing, while attaining the physical relevancy of the results.

**Keywords** Arbitrary Lagrangian-Eulerian (ALE) · spurious mixing · adaptive mesh · non-hydrostatic · internal solitary waves · ocean model

## 1 Introduction

Since the mid-20<sup>th</sup> century, numerical models have become indispensable tools for analyzing and predicting oceanic systems and processes. As a result, considerable research has focused on developing discretization methods that faithfully simulate physical phenomena while minimizing numerical artifacts. Among these artifacts, spurious numerical mixing/diffusion remains a well-known and persistent issue.

Spurious mixing is a frequent phenomenon in ocean models that occurs due to the numerical diffusion introduced by the spatial discretization of advection terms. The most common occurrence of this, is in the case of Spurious Diapycnal Mixing (SDM), in which vertical advection introduces mixing across the density layers thus severely altering the stratification. Consequently, various methods to track and remedy SDM have been proposed. The two main approaches center around designing low dissipation advection schemes and exploiting vertical coordinate systems [2, §2.3.2]. The present paper aims to contribute towards the latter direction.

The choice of vertical coordinate is a crucial aspect in the design of numerical ocean models, and consequently, a substantial body of research has focused on this topic. Following [3], the three vertical coordinate systems that are traditionally used within the oceanographic community are of the  $z, \rho$  and  $\sigma$  nature. All of the above fall within the Generalized Vertical Coordinate (GVC) framework introduced by Starr [4] that is often used to map the physical space into a conveniently bounded parametric domain.

Each one of the GVC's has its own corresponding advantages and drawbacks and thus the choice among them is not always an obvious one. This led to the introduction of a hybrid  $\rho/z$ -model by Bleck [5], in which a remeshing technique

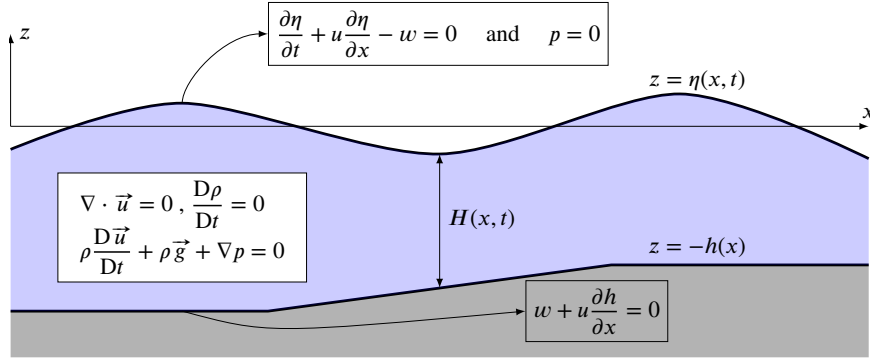


Figure 1: The free-surface Euler system

on the fixed  $z$ -grid is performed when a layer's thickness approaches zero and consequently the layers are redefined. This Vertically Lagrangian-Remap (VLR) technique has been used with success in the HYCOM [6] model, and has been incorporated in the MOM6 [7] and POM [8] ocean models (originally using  $z$  and  $\sigma$  coordinates respectively [9, 10]).

The versatility of such GVC approaches gives rise to a large number of ocean models with vertical coordinates that are designed within the Arbitrary Lagrangian Eulerian (ALE) framework. For an extensive review of recent developments in VLR/ALE schemes in ocean models, the reader is referred to [11]. One of the basic advantages of this ALE framework is the flexibility it gives to exploit the vertical mesh movement to achieve specific requirements. For example in [12] and [13], vertical ALE coordinates were added to NEMO and MPAS respectively to reduce SDM through a superposition of imposed motions (barotropic, high/low frequency baroclinic modes, additional smoothing terms e.t.c.). Similar approaches appear also in [14, 15, 16].

Having all the above as inspiration, in this work we aim to present a comprehensive compact mesh-moving ALE method with the goal to reduce SDM. The proposed methodology is introduced to SLS; a nonhydrostatic ALE solver introduced by the authors in [1]. SLS is built upon a fully versatile GVC framework that defines the vertical grid motion through a Geometric Conservation Law (GCL). The equations are discretized using a second order Finite Volume (FV) method, while the nonhydrostatic pressure is calculated using a Poisson equation in an operator splitting fashion.

In [1], SLS was tested and validated on single-density nonhydrostatic free-surface flows. In the present paper, we present improvements on the numerical scheme alongside the novel variational ALE mesh movement. The scheme is enhanced with various additions, including a second order layer reconstruction that -alongside the proposed discrete hydrostatic gradient- results in a well-balanced robust scheme. Additionally, entropy stable fluxes are utilized, while the Poisson equation is solved within the Finite Element framework.

The main innovation of the paper concerns the vertical mesh movement that is a central feature of the formulation of SLS. This novel mesh movement is prescribed through a multi-objective optimization that is compactly described by a cost functional. The functional is minimized in the spirit of calculus of variations, giving rise to an elliptic equation that can be efficiently solved numerically. To bolster the utility of the proposed method, the various weighting factors are analyzed and specific values are laid out. While this approach is not restricted to specific objectives, herein we aim to effectively reduce SDM while maintaining the physical relevance of the results.

The paper is structured as follows: In §2, the equations in the GVC framework are laid out, while in §3 the numerical scheme is presented. In §4, the variational mesh movement is derived, alongside the analysis of the weighting factors in §4.4 and §4.5. Lastly, in §5 results of the method are presented.

The numerical test cases center around Internal Solitary Waves (ISWs), since they are highly nonlinear and inherently nonhydrostatic, making them a valuable benchmark for SLS. In particular, ISW-topography interactions are highly transient and induce rapid, strong deformations of the isopycnals, which can provide a formidable test for mesh-moving formulations with a Lagrangian bias. This, combined with the practical relevance of ISWs in regional dynamics (see [17]), offers an appealing benchmark to assess whether the proposed variational mesh movement can robustly reduce spurious diapycnal mixing (SDM) even in such demanding cases.

## 2 Theoretical Formulation

Let us consider a domain vertically bounded by the bottom  $z = -h(x)$  and the free-surface  $z = \eta(x, t)$  that are considered to be single-valued functions of the horizontal coordinate  $x$  (see Fig.1). Inside the domain the motion is governed by the Euler equations for an incompressible fluid of variable density  $\rho$ . The bottom and the free-surface are considered as material surfaces and a zero pressure condition is enforced on the latter. On the lateral boundaries, we consider either Neumann (inviscid wall) or Dirichlet boundary conditions based on the case at hand.

### 2.1 The Generalized Vertical Coordinate system

In order to formulate the Free-Surface Euler system in Generalized Vertical Coordinates, a projection of the following type is assumed:

$$z = -h(x') + \int_0^\xi L(x', \xi, t') d\xi , \quad \text{with} \quad x = x' , t = t' \quad (1)$$

Thus,  $z$  is replaced by the parametric coordinate  $\xi \in [0, 1]$  while  $x, t$  remain unchanged. By definition,  $\xi = 0$  corresponds to the bottom boundary and we chose that  $\xi = 1$  maps to the free-surface by choosing that  $\int_0^1 L d\xi = H \stackrel{\text{def}}{=} \eta + h$ . The quantity  $L$  is the determinant of the transformation's Jacobian matrix and represents the amount of physical space that is contained within a control volume in the parametric space:  $dV = L dx d\xi$  (see Fig.2).

Note that for a fixed  $\xi$ ,  $z(x, \xi, t)$  represents a surface that evolves in time. Thus, discretization along the  $\xi$  axis yields a set of surfaces  $z(x, \xi_j, t)$ , which, following common practice in ocean modeling, we refer to as layers.

If we transform the Euler system in GVC coordinates (see also Appendix A of [1]) and split the pressure as usual into the hydrostatic  $p_h$  and the nonhydrostatic components  $p = p_h + q = \int_z^\eta \rho g dz + q$  we get:

$$\frac{\partial L}{\partial t} + \frac{\partial}{\partial x}(Lu) + \frac{\partial \vartheta}{\partial \xi} = 0 \quad (2a)$$

$$\frac{\partial}{\partial t}(L\rho) + \frac{\partial}{\partial x}(L\rho u) + \frac{\partial}{\partial \xi}(\vartheta\rho) = 0 \quad (2b)$$

$$\frac{\partial}{\partial t}(LV) + \frac{\partial}{\partial x}(LuV) + \frac{\partial}{\partial \xi}(\vartheta V) + \frac{L}{\rho} (\rho g + \mathbf{grad} p_h + \mathbf{grad} q) = 0 \quad (2c)$$

$$\operatorname{div} \mathbf{V} = 0 \quad (2d)$$

With  $\mathbf{grad}(\cdot) \stackrel{\text{def}}{=} [\operatorname{grad}_x(\cdot), \operatorname{grad}_z(\cdot)]^T$  and  $\operatorname{div}(\cdot) \stackrel{\text{def}}{=} \operatorname{grad}_x(\cdot) + \operatorname{grad}_z(\cdot)$  we refer to the differential operators on the physical plane. The velocity field is  $\mathbf{V} = [u, w]^T$  whereas  $\vartheta$  is the vertical contravariant velocity:

$$\vartheta \stackrel{\text{def}}{=} w - u \frac{\partial z}{\partial x} - \frac{\partial z}{\partial t} \quad (3)$$

Even though we can solve these fully nonlinear equations, there is also the option to solve the system under the Boussinesq approximation where the pressure gradients are divided with a constant reference density:  $\frac{1}{\rho} \mathbf{grad} p_h \rightarrow \frac{1}{\rho_0} \mathbf{grad} p_h$  and  $\frac{1}{\rho} \mathbf{grad} q \rightarrow \frac{1}{\rho_0} \mathbf{grad} q$ . When such an approximation is used, it will be noted.

Gathering all the above, we can write the system in compact form:

$$\frac{\partial}{\partial t}(\mathbf{U}) + \frac{\partial}{\partial x}\mathbf{F}(\mathbf{U}) + \frac{\partial}{\partial \xi}\mathbf{G}(\mathbf{U}; \vartheta) + \frac{1}{\rho}(\mathbf{B} + \mathbf{Q}) = 0 \quad (4a)$$

$$\operatorname{div} \mathbf{V} = 0 \quad (4b)$$

where  $\mathbf{F}(\mathbf{U}) \stackrel{\text{def}}{=} u\mathbf{U}$  and  $\mathbf{G}(\mathbf{U}; \vartheta) \stackrel{\text{def}}{=} \frac{\vartheta}{L}\mathbf{U}$  are the horizontal and vertical advection fluxes respectively. With  $\mathbf{B}$  and  $\mathbf{Q}$  we note the hydrostatic and nonhydrostatic gradient terms:

$$\mathbf{B} = \begin{bmatrix} \mathbf{0} \\ \rho g L + L \mathbf{grad} p_h \end{bmatrix} = \begin{bmatrix} 0 \\ 0 \\ L \operatorname{grad}_x p_h \\ 0 \end{bmatrix} , \quad \mathbf{Q} = \begin{bmatrix} \mathbf{0} \\ L \mathbf{grad} q \end{bmatrix} = \begin{bmatrix} 0 \\ 0 \\ L \operatorname{grad}_x q \\ L \operatorname{grad}_z q \end{bmatrix} \quad (5)$$

Throughout the paper we note the conservative variables as  $\mathbf{U} \stackrel{\text{def}}{=} [L, L\rho, Lu, Lw]^T$ , whereas the primitive ones with  $\mathbf{U}^p \stackrel{\text{def}}{=} [L, \rho, u, w]^T$ .

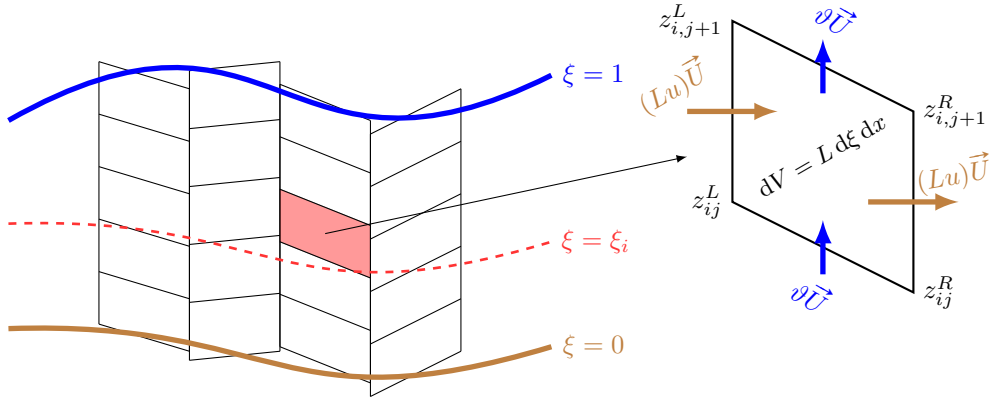


Figure 2: The Finite Volume scheme with the reconstructed non-conforming mesh.

### 2.1.1 The Geometric Conservation Law and ALE formulation

Before proceeding, we must highlight the role of the so-called Geometric Conservation Law (GCL), which is here expressed in eq.(2a). Essentially, the GCL enforces the compatibility between the volume fluxes  $Lu d\xi$  and  $\vartheta dx$  and the volume expansion  $dx d\xi \frac{\partial L}{\partial t}$  (see Fig.2). If one prescribes  $\vartheta$  then eq.(2a) can be used to evolve  $L$  in a conservative way (see [1]). Thus, the mesh movement algorithm boils down to choosing the velocity  $\vartheta$ .

### 2.2 Timestepping

Let us consider the time steps  $[t^n, t^{n+1}]$ . Since the system includes a div-free constraint (eq.2d), we employ the classic second order pressure-correction scheme [18]:

- **Step 1:** Advance eq.(2a)-(2c), using  $q \approx q^n$  and get the mid-step values:

$$\mathbf{U}^* = \mathbb{T} [\mathbf{R}(\cdot, q^n), \mathbf{U}^n, \Delta t^n] \quad (6)$$

Where  $\mathbb{T}$  can be any discrete time-stepping operator (herein, a classic 4<sup>th</sup> order Runge-Kutta is adopted) that is applied to the residual:

$$\mathbf{R}(\mathbf{U}; q^n) = -\frac{\partial}{\partial x} \mathbf{F}(\mathbf{U}) - \frac{\partial}{\partial \xi} \mathbf{G}(\mathbf{U}, \vartheta(\mathbf{U})) - \frac{1}{\rho} \mathbf{B}(\rho, L) - \frac{1}{\rho} \mathbf{Q}^n \quad (7)$$

- **Step 2:** Correct the pressure and velocity fields in accordance to:

$$\frac{\mathbf{V}^{n+1} - \mathbf{V}^*}{\Delta t} + \frac{1}{\rho^*} \mathbf{grad}(q^{n+1} - q^n) = 0 \quad (8a)$$

$$\operatorname{div} \mathbf{V}^{n+1} = 0 \quad (8b)$$

By combining eq.(8a) and eq.(8b), one arrives at a standard pressure-Poisson equation.

## 3 Numerical Framework

We discretize the parametric space into  $n_x \times n_l$  orthogonal cells  $\bigcup_{ij} [x_i, x_{i+1}] \times [\xi_j, \xi_{j+1}]$ . The velocities  $u, w$  and the variables  $\rho, L$  are considered to be cell-centered, while  $\vartheta$  is placed on the horizontal faces. We choose this placement of  $\vartheta$  so that it is collocated with the flux  $\mathbf{G}$ .

### 3.1 Explicit terms

By considering the FV fluxes as shown in Fig.2 we get the following discretization for eq.(7) on the cell of parametric area  $|\Omega_{ij}| = \Delta x_i \times \Delta \xi_j$ :

$$-\mathbf{R}_{ij} |\Omega_{ij}| = \Delta \xi_j \left[ \mathbf{F}_{i+\frac{1}{2},j} - \mathbf{F}_{i-\frac{1}{2},j} \right] + \Delta x_i \left[ \mathbf{G}_{i,j+\frac{1}{2}} - \mathbf{G}_{i,j-\frac{1}{2}} \right] + \frac{|\Omega_{ij}|}{\rho_{ij}} (\mathbf{B}_{ij} + \mathbf{Q}_{ij}) \quad (9)$$

In order to extract the face-based values, the primitive variables are reconstructed using an 1D MUSCL-type TVD procedure [19] applied on the  $x$  and  $\xi$  directions independently. Specifically, a piecewise linear reconstruction coupled with the Superbee limiter is employed [20]. The reconstructed variables at the vertical faces are noted as  $\mathbf{U}^{L/R}$ , whereas on the horizontal ones as  $\mathbf{U}^{+/-}$  (see Fig.3.)

The fluxes  $\mathbf{F}, \mathbf{G}$  on the vertical and horizontal faces are computed using approximate flux solvers. The hydrostatic gradient is based on a nonconservative cell-face approach, whereas the nonhydrostatic gradient is calculated within the FEM framework presented in §3.2.

### 3.1.1 Layer reconstruction

As described in §2.1.1, SLS exactly satisfies the GCL and thus  $L_{ij}$  are evolved through eq.(2a) as an independent variable. Although this restricts the cells' volume to be  $\Delta V_{ij} = L_{ij} \Delta \xi_j \Delta x_i$ , the cells' exact shape is not fully prescribed. Consequently, a reconstruction procedure of the type  $L_{ij} \mapsto z_{ij}^L, z_{ij}^R$  (see Fig.2) is needed in order to get the cells' physical shape.

In the present, we apply the layer reconstruction described in [21], where the approach of [22] is extended to the multilayer case. The method of [22] is volume-conserving and utilizes partially dry cells, i.e. cells that leave part of the bottom topography exposed. Herein, each layer is reconstructed separately and then, if the layers clash each other, a correction is applied. The result is a mesh where the top and bottom of the quadrilaterals is linear with piecewise constant gradients  $(z_x)_{i,j}$  (see Fig.2).

This method is robust and well-balanced in the sense that in the lake-at-rest configuration, the reconstructed gradients are zero:  $(z_x)_{i,j} \equiv 0$ . (see [21]).

### 3.1.2 Hydrostatic pressure gradient

Another thing that must be addressed is the discrete hydrostatic pressure gradient term. Specifically, due to the density stratification, the scheme must correctly capture the variable density hydrostatic effects, on a mesh where the variables are discontinuous across cells. Additionally, in the case of our system, this hydrostatic gradient term is in nonconservative form:

$$L\text{grad}_x p_h = L \frac{\partial p_h}{\partial x} - \frac{\partial z}{\partial x} \frac{\partial p_h}{\partial \xi} = L \left( \frac{\partial}{\partial x} \int_{\xi}^1 \rho L d\xi + \rho \frac{\partial z}{\partial x} \right) \quad (10)$$

In order to treat this properly, we split the gradient into cell and face contributions as it is customary for the single layer case [23, 24]:

$$\Delta x_i B_{ij} = \frac{1}{2} (1 + a_{i+1/2,j}) B_{i+1/2,j}^{face} + B_{ij}^{cell} + \frac{1}{2} (1 - a_{i-1/2,j}) B_{i-1/2,j}^{face} \quad (11)$$

where  $a_{i+1/2,j}$  are face-based coefficients that introduce upwinding. Herein, we adopt and central approach with  $a_{i+1/2,j} \equiv 0$ . The term  $B_{ij}^{cell}$  accounts for the reconstruction within the cell while  $B_{i+1/2,j}^{face}$  for the jumps across its faces.

Thus, we calculate based on eq.(10):

$$B_{ij}^{cell} = L_{ij} \Delta x_i \left[ \left( \sum_{k=j+1}^{n_l} \rho_{ik} g [(z_x)_{i,k+1} - (z_x)_{ik}] \right) + g \rho_{ij} (z_x)_{ij} \right] \quad (12)$$

$$B_{i+1/2,j}^{face} = \underbrace{\left( \frac{L_L + L_R}{2} \right)_{i+1/2,j} \left[ (p_R - p_L) + g \frac{\rho_R + \rho_L}{2} (z_R - z_L) \right]_{i+1/2,j}}_{\delta p_{i+1/2,j}} \quad (13)$$

where  $\rho_L = \rho_{ij}$  and  $\rho_R = \rho_{i+1,j}$  are low order approximations on the face and the rest are given by:

$$(p_{L/R})_{i+1/2,j} = \sum_{k=j+1}^{n_l} g (\rho_{L/R} L_{L/R} \Delta \xi)_{i+1/2,k} + \frac{1}{2} g (\rho_{L/R} L_{L/R} \Delta \xi)_{i+1/2,j} \quad (14)$$

$$(z_{L/R})_{i+1/2,j} = -h_{i+1/2} + \sum_{k=1}^{j-1} (L_{L/R} \Delta \xi)_{i+1/2,k} + \frac{1}{2} (L_{L/R} \Delta \xi)_{i+1/2,j} \quad (15)$$

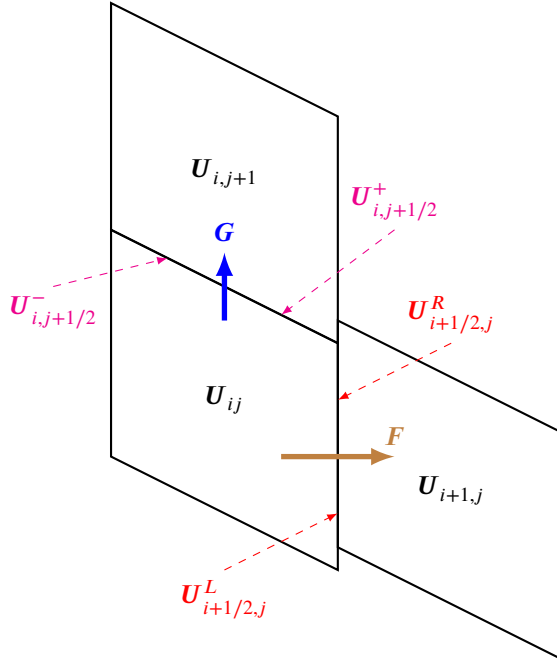


Figure 3: Sketch of the Finite Volume fluxes, alongside the reconstructed variables on the cell's faces:  $\vec{U}^{L/R}$  and  $\vec{U}^{+/-}$ .

Note that this discretization alongside the hydrostatic reconstruction of the previous section results in a well-balanced scheme, since if all the layers are horizontal then  $(z_x)_{i,j} \equiv 0$ ,  $\delta p_{i+1/2,j} \equiv 0$  and thus the above relation is identically zero and the lake-at-rest equilibrium is satisfied.

### 3.1.3 Flux solvers

For the discretization of the horizontal advection fluxes we utilize the entropy stable framework (see e.g. [25]). Thus, the numerical fluxes are:

$$(Lu)_{\text{vertical face}} \approx F_{i+\frac{1}{2}}^L = \bar{Lu} - \frac{c_{\text{bar}}}{2} \frac{\delta p_{i+\frac{1}{2}}}{g\rho} - \frac{|\bar{u}|}{2} (L_R - L_L) \quad (16a)$$

$$(Lu^2)_{\text{vertical face}} \approx F_{i+\frac{1}{2}}^{Lu} = \bar{Lu} \times \bar{u} - \bar{L} \frac{|\bar{u}| + c_{\text{bar}}}{2} (u_R - u_L) \quad (16b)$$

$$(Luw)_{\text{vertical face}} \approx F_{i+\frac{1}{2}}^{Luw} = \bar{Lu} \times \bar{w} - \bar{L} \frac{|\bar{u}| + c_{\text{bar}}}{2} (w_R - w_L) \quad (16c)$$

where  $\bar{(\cdot)} = ((\cdot)_R + (\cdot)_L)/2$  and the barotropic speed is  $c_{\text{bar}} = \sqrt{gH}$ .

The choice of these entropy fluxes is motivated by their good behavior with regard to energy stability. They are constructed based on the knowledge that the entropy variables of the multilayer system are  $\mathbf{U}^e = [p, u, w]^T$  [25], and thus terms like  $\mathbf{A}(\mathbf{U}_R^e - \mathbf{U}_L^e)$  result in a reduction of the system's mechanical energy if  $\mathbf{A}$  is a negative definite matrix [26]. The jump of the entropy variables is scaled according to the maximum eigenvalue of the system  $|u| + \sqrt{gH}$  (the barotropic one). This results in a robust numerical scheme that is both a) energy-stable and b) well-balanced even at the wet-dry fronts. Aside from these terms, a simple upwinding term  $\frac{1}{2}|\bar{u}|(L_R - L_L)$  is added to the GCL flux so that wiggles are negated.

For the vertical advection of all conserved variables and for the horizontal  $\rho$  flux (or any other tracer) we simply employ an upwinding based the GCL fluxes:

$$(L\rho u)_{\text{vertical face}} \approx F_{i+\frac{1}{2}}^{L\rho} = F_{i+\frac{1}{2}}^L \times \begin{cases} \rho_L & , F_{i+\frac{1}{2}}^L > 0 \\ \rho_R & , F_{i+\frac{1}{2}}^L < 0 \end{cases} \quad (17)$$

$$(\vartheta \mathbf{U}_p)_{\text{horizontal face}} \approx \mathbf{G}_{j+\frac{1}{2}} = \vartheta_{j+\frac{1}{2}} \times \begin{cases} \mathbf{U}_{j+\frac{1}{2}}^{p,-} & , \vartheta_{j+\frac{1}{2}} > 0 \\ \mathbf{U}_{j+\frac{1}{2}}^{p,+} & , \vartheta_{j+\frac{1}{2}} < 0 \end{cases} \quad (18)$$

Note that these fluxes for the tracer  $\rho$  are in line with the Consistency with Continuity concept [27], in the sense that if  $\rho = \text{const}$ , then this reduces to the GCL multiplied by  $\rho$  and the advection scheme preserves the constancy of tracers.

### 3.2 Nonhydrostatic pressure correction

What remains is to propose a numerical scheme for the pressure correction of eq.(8). For this, we derive the weak formulation of the div-free condition in order to solve it in the framework of the Finite Element Method. For its discretization, we utilize the classic linear nodal Q4 elements on the  $x - \xi$  plane. This procedure is presented in Appendix A. If we define  $\phi_{ij} \stackrel{\text{def}}{=} \Delta t(q_{ij}^{n+1} - q_{ij}^n)$ , where  $q_{ij}$  are values of the dynamic pressure at the nodes  $(x_i, \xi_j)$  of the quadrilaterals, we arrive at the following linear system:

$$\mathbf{K}\phi = \mathbf{G}^x \mathbf{u}^* + \mathbf{G}^z \mathbf{w}^* - \mathbf{B}\mathbf{v}_{bc} \quad (19)$$

with  $\mathbf{K}$  being the classic stiffness matrix, whereas  $\mathbf{G}^x, \mathbf{G}^z, \mathbf{B}$  correspond to suitable integrals of the Q4 shape functions over the domain and its boundary.

After solving the linear system for  $\phi$  we can then update the velocity and pressure field using eq.(8b):

$$\mathbf{u}^{n+1} = \mathbf{u}^* - \frac{(\mathbf{G}^x)^T \phi}{L\Delta x \Delta \xi} \quad (20a)$$

$$\mathbf{w}^{n+1} = \mathbf{w}^* - \frac{(\mathbf{G}^z)^T \phi}{L\Delta x \Delta \xi} \quad (20b)$$

$$q^{n+1} = q^n + \frac{\phi}{\Delta t} \quad (20c)$$

where the division is considered to be element-wise.

### 3.3 Wetting-drying and positivity preservation

The last thing to specify is the treatment of the wetting-drying of cells. If the cells tend to dry ( $L \rightarrow 0$ ), then one cannot get the primitive variables  $u, w, \rho$  from their conservative counterparts  $Lu, Lw, L\rho$  without sacrificing numerical stability. Following the standard practices, we set two tolerances  $\epsilon_{vel}, \epsilon_\rho$  so that if  $L$  is below these, we set  $u = w = 0$  and the density is retained at its pre-drying value. For all the present simulations, we set  $\epsilon_{vel} = 10^{-3}$  and  $\epsilon_\rho = 10^{-6}$ .

Additionally, in the FEM solver, cells with  $L < \epsilon_{vel}$  are considered dried and the condition imposed on them is that the pressure on the top and bottom sides are equal:  $q_{i,j+1} = q_{i,j}$  and  $q_{i+1,j+1} = q_{i+1,j}$ , thus avoiding any singularities when constructing the stiffness matrix.

Another thing to be addressed is that the advection scheme must keep the cell's volume positive:  $L \geq 0$ . In order to directly enforce that, we use the approach presented in [28]:

- For each cell we compute the following:  $s_{ij} = \frac{\Delta t}{L_{ij}\Delta x_i} \left( \max\{F_{i+1/2,j}^L, 0\} + \max\{-F_{i-1/2,j}^L, 0\} \right)$
- For each face, if  $F_{i+1/2,j}^L > 0$  multiply all advection fluxes  $F_{i+1/2,j}$  with  $\min\{s_{ij}, 1\}$ , otherwise multiply them with  $\min\{s_{i+1,j}, 1\}$

This ensures positivity without imposing time-step or any other restrictions on the method. The exact same procedure is also used on the vertical fluxes.

## 4 ALE movement

In the introductory section, it was noted that the main idea behind the ALE/VLR methodologies is not only to reduce numerical mixing (usually done by considering an isopycnal-type configuration) but also retain the advantages of other coordinate systems ( $z/\sigma$ ). Within this section we will describe the definition of the ALE motion that blends all these objectives.

### 4.1 Mesh adaptation

As was briefly mentioned in §1, adaptive mesh algorithms already exist in the literature of ocean models. The distinctive characteristic of our proposed variational mesh movement is that it is derived through the minimization of a cost functional, thus satisfying an optimality criterion. That being said, the ALE strategies considered herein (Lagrangian bias, smoothing and refinement) have been used in previous works [16] and their effectiveness has been demonstrated. Specifically, in [29], a monitor function closely resembling eq.(36) has been used in the context of a Discontinuous Galerkin (DG) ocean model, while in [16] smoothing through diffusion operators is used alongside similar monitor function ideas.

The proposed method aims to gather all these ideas into a compact and consistent mathematical formulation. By doing so, we are able to perform the analysis demonstrated in §4.4,§4.5 and propose how the various target objectives should blend. This analysis is also bolstered by the application of the variational mesh movement in challenging nonhydrostatic flows (§5). Concluding, the derivation of the movement, the analysis of the coefficients and the numerical investigation, aspires to propose a new framework to design mesh movement in ALE models and provide insights into already existing methodologies.

### 4.2 Numerical mixing

Spurious (numerical) mixing is generally attributed to the diffusive character of the advection scheme, and it has been the topic of many studies within the oceanographic community [2]. In order to quantify the amount of diffusion introduced by the numerical scheme we consider the following: For an incompressible fluid, in the absence of boundary fluxes, we have the conservation property  $\frac{d}{dt} \iiint \rho^2 dV = 0$ . This conservation principle in general is not satisfied by the discrete scheme due to the diffusive nature of the numerical fluxes. Therefore, to quantify spurious numerical mixing (SDM), we will study how  $\iiint \rho^2 dV$  decays in time [30].

For the vertical advection, if the reconstruction is piecewise constant, the following rate of decay for the discrete  $\iiint \rho^2 dV$  holds:

$$\frac{d}{dt} \sum_j (\Delta \xi_j) L_j \rho_j^2 = - \sum_j |\vartheta_{j+1/2}| (\rho_{j+1} - \rho_j)^2 \quad (21)$$

The algebraic steps to reach eq.(21) are presented in Appendix B. However, in the case of SLS, a second order (linear) reconstruction scheme is utilized (see §3.1) and thus the above equation is not exact. Despite this, we will focus on the above equation since it captures adequately the basic concepts of numerical diffusion, as seen in Fig.11 of the results.

From this analysis, it becomes evident that spurious mixing primarily depends on the vertical mesh velocity  $\vartheta$  and on the density contrast across adjacent layers. Consequently, our strategy to mitigate spurious numerical diffusion focuses on controlling these two quantities when constructing the ALE mesh motion. Based on eq.(21), we identify two possible approaches to reduce spurious mixing: (a) limit the magnitude of  $\vartheta$ , thereby enforcing a motion that tends to follow isopycnal surfaces and minimizes cross-isopycnal transport, or (b) reduce the interfacial density jump  $\rho_{j+1} - \rho_j$ , which decreases the intensity of spurious mixing driven by numerical diffusion across density interfaces.

To further investigate this, we write:

$$\rho_{j+1} - \rho_j = \left. \frac{\partial \rho}{\partial z} \right|_{j+1/2} \frac{\Delta z_{j+1} + \Delta z_j}{2} + \mathcal{O}(\Delta z^2) \approx \frac{\partial \rho}{\partial z} \Delta z \quad (22)$$

Namely, to minimize this term, we need cells with increased vertical resolution in areas with large density gradients and thus we aim to also incorporate this into the method.

### 4.3 Optimization process and variational formulation

Our approach is to gather all the different target objectives and then construct an appropriate optimization problem. Also, based on the discussion of the previous paragraph we will add an additional term that will help reduce spurious mixing. Specifically, we want to:

- Minimize  $\vartheta^2$ , so that the vertical mass transfer is limited: this introduces a Lagrangian tendency.
- Minimize the gradients  $\left(\frac{\partial}{\partial x}(z - z_{ref})\right)^2$  and  $\left(\frac{\partial}{\partial \xi}(z - z_{ref})\right)^2$ : this smoothens out the mesh and skews it towards a reference configuration  $z_{ref}$ . This can be of any desired type (like a  $z/\rho$  model). Herein, a  $\sigma$  reference grid will be used for all examples:  $z_{ref} = -h + \xi H$
- Minimize  $\left(M \frac{\partial z}{\partial \xi}\right)^2$ : this distributes more mesh points where the function  $M(x, \xi) \geq 0$  is larger. If  $M \propto \left|\frac{\partial \rho}{\partial z}\right|$ , this distributes the mesh so that the right hand side (RHS) of eq.(21) is reduced.

The function  $M$  essentially offers the opportunity to design the spacing of the mesh according to user-defined criteria. These terms are called *monitor functions* and are heavily used in variational mesh adaptation [31, 32]. Having these techniques as inspiration, we propose an optimization procedure that reduces SDM within framework of ALE ocean models.

Specifically, we aim to satisfy a combination of these target-objectives within each time-step. To begin with, suppose that at the start of each timestep the layers are positioned at  $z^n(x, \xi, t) = -h(x) + \int_0^\xi L^n(x, \xi, t) d\xi$ . Starting from this, we define the ALE layer movement so that at the final positions  $z^{n+1}(x, \xi, t)$  the above optimality criteria are enforced.

The evolution of the layers' positions is dictated by the GCL, which reads:

$$(2a) \Rightarrow \frac{L^{n+1} - L^n}{\Delta t} + \frac{\partial}{\partial x}(Lu)^* + \frac{\partial \vartheta}{\partial \xi} = 0 \Rightarrow z^{n+1} = z^n - \underbrace{\Delta t \int_0^\xi \frac{\partial}{\partial x}(Lu)^* d\xi}_{z_{lag}^*} - \Delta t \cdot \vartheta \quad (23)$$

Thus, we see that  $\vartheta$  acts as a correction on the Lagrangian impulse  $R_{lag} \stackrel{\text{def}}{=} -\int_0^\xi \frac{\partial}{\partial x}(Lu)^* d\xi$ . As a result, we can regulate the evolution of  $z(x, \xi, t)$  by prescribing  $\vartheta(x, \xi, t)$  in a suitable manner.

Based on the objectives described above, the following cost functional is proposed:

$$\mathcal{F}(\vartheta) = \iiint \left[ \underbrace{T_{ref} a_\vartheta \vartheta^2}_{\text{Lagrangian}} + \underbrace{a_x \frac{\Delta x^2}{\Delta t} \left( \frac{\partial}{\partial x}(z^{n+1} - z_{ref}) \right)^2}_{\text{Smoothing}} + \underbrace{a_\xi \frac{\Delta \xi^2}{\Delta t} \left( \frac{\partial}{\partial \xi}(z^{n+1} - z_{ref}) \right)^2}_{\text{Monitor function}} + a_M \frac{\Delta \xi^2}{\Delta t} \left( M \frac{\partial z^{n+1}}{\partial \xi} \right)^2 \right] dx d\xi \quad (24)$$

or in tensorial notation:

$$\mathcal{F}(\vartheta) = \iiint \left[ T_{ref} a_\vartheta \vartheta^2 + \frac{1}{\Delta t} \|\mathbf{A}_S \nabla(z^{n+1} - z_{ref})\|^2 + \frac{1}{\Delta t} \|\mathbf{A}_M \nabla z^{n+1}\|^2 \right] dx d\xi \quad (25a)$$

$$\text{where: } \mathbf{A}_S = \begin{bmatrix} \sqrt{a_x} \Delta x & 0 \\ 0 & \sqrt{a_\xi} \Delta \xi \end{bmatrix} \quad \text{and} \quad \mathbf{A}_M = \begin{bmatrix} 0 & 0 \\ 0 & \sqrt{a_M} \Delta \xi M \end{bmatrix} \quad (25b)$$

with  $\nabla \stackrel{\text{def}}{=} \left[ \frac{\partial}{\partial x}, \frac{\partial}{\partial \xi} \right]^T$  being the gradient operator on the  $x - \xi$  plane.

The coefficients  $a_\vartheta, a_x, a_\xi$  are non-dimensional, whereas  $a_M$  must be carefully chosen based on the form of  $M$ . The modeler has the freedom to specify these four parameters based on the particular configuration under study. Below, it will be shown how these four values should blend.

$T_{ref}$  represents a characteristic time scale. Since this study concerns the evolution waves in stratified flows, we chose  $T_{ref} = \sqrt{h/g'}$  where the reduced gravity is given by  $g' \stackrel{\text{def}}{=} g(\rho_{max} - \rho_{min})/\rho_0$ .

Gathering all these, the optimization problem states:

$$\text{find } \vartheta \in \mathcal{V} \quad \text{so that} \quad \mathcal{F}(\vartheta) = \min_{\vartheta_* \in \mathcal{V}} \{\mathcal{F}(\vartheta_*)\}$$

where  $\mathcal{V}$  is a suitable function space. Through the framework of the calculus of variations, in Appendix C we conclude that  $\vartheta$  obeys the following:

$$a_\vartheta \frac{T_{ref}}{\Delta t} \vartheta - \nabla \cdot \left[ \mathbf{A}_S^2 \nabla (\vartheta - v_{lag}) + \mathbf{A}_M^2 \nabla \left( \vartheta - \frac{z_{lag}^*}{\Delta t} \right) \right] = 0 \quad (26)$$

where  $v_{lag} \stackrel{\text{def}}{=} \frac{z_{lag}^* - z_{ref}}{\Delta t}$ . The expression in eq.(26) is a Helmholtz equation on the  $x - \xi$  plane and can be solved efficiently using standard numerical methods.

To better understand eq.(26), we can reformulate it by substituting  $z^{n+1} = z^n + \Delta t(R_{lag} - \vartheta)$  that results in:

$$T_{ref} \frac{z_{n+1} - z_n}{\Delta t} = T_{ref} R_{lag} + \nabla \cdot [\mathbf{A}_S^2 \nabla (z^{n+1} - z_{ref}) + \mathbf{A}_M^2 \nabla z^{n+1}] \quad (27)$$

In order to balance these 4 coefficients, the analysis is divided into two parts. First, we will describe the interaction of  $a_\vartheta$  with  $a_x, a_\xi$  followed by the balance between  $a_M$  and  $a_\xi$ .

#### 4.4 The variational minimizer as a frequency filter

Firstly, we aim to balance the Lagrangian and smoothing terms. To do so, let  $a_M = 0$  and  $a_x = a_\xi = a_{x\xi}$ . Then, all coefficients in eq.(27) are constant and thus Fourier analysis can be performed based on a space/time expansion of the type:

$$z = \sum_{\{\omega, k_x, k_\xi\}} \hat{z}_{\{\omega, k_x, k_\xi\}} \exp(i\omega t + ik_x x + ik_\xi \xi) \quad (28)$$

with  $i \stackrel{\text{def}}{=} \sqrt{-1}$ . Inserting this into eq.(27) and supposing that  $\Delta t$  is small enough so that  $\frac{z^{n+1} - z^n}{\Delta t} \rightarrow \frac{\partial z}{\partial t}$  we get:

$$ia_\vartheta (\omega T_{ref}) \hat{z} = a_\vartheta T_{ref} \hat{R}_{lag} - a_{x\xi}(k_*)^2 (\hat{z} - \hat{z}_{ref}) \quad (29)$$

where  $k_* \stackrel{\text{def}}{=} \sqrt{(k_x \Delta x)^2 + (k_\xi \Delta \xi)^2}$  is the combined non-dimensional wavenumber.

If, in addition, we define  $\omega_* \stackrel{\text{def}}{=} \omega T_{ref}$  and  $\hat{z}_{lag} \stackrel{\text{def}}{=} \hat{R}_{lag}/(i\omega)$ , we get:

$$\hat{z} = \frac{(a_\vartheta i\omega_*) \hat{z}_{lag} + (a_{x\xi} k_*^2) \hat{z}_{ref}}{(a_\vartheta i\omega_*) + (a_{x\xi} k_*^2)} \quad (30)$$

According to eq.(30), the ratio between  $a_\vartheta$  and  $a_{x\xi}$  dictates how aggressively the high wavenumber spatial Lagrangian modes are damped. Also note that with respect to the time frequency, higher  $\omega_*$  favor the Lagrangian term  $\hat{z}_{lag}$ . Consequently, the mesh follows the fast Lagrangian motions that are prescribed by the horizontal fluxes, while smoothing slow motions.

In order to balance  $a_\vartheta$  and  $a_{x\xi}$ , we study the ratio between the Lagrangian and smoothing terms for the case of  $\omega_* = 2\pi$ , i.e. motions that have a period equal to the reference one. Since all the functions are defined on a grid with spacings  $\Delta x, \Delta \xi$ , the highest wavenumbers that can be expected are the Nyquist ones:  $k_x \leq \pi/\Delta x$  and  $k_\xi \leq \pi/\Delta \xi$ . This corresponds to  $k_* \leq \pi = k_{\text{Nyquist}}$ . Based on this, the ratio for  $T = T_{ref}$  is:

$$(30) \Rightarrow \frac{\text{Lagrangian amplitude}}{\text{Smoothing amplitude}} = \frac{a_\vartheta \omega_*}{a_{x\xi} k_*^2} = \frac{a_\vartheta}{a_{x\xi}} \times \frac{2}{\pi} \times \left( \frac{k_{\text{Nyquist}}}{k_*} \right)^2 \quad (31)$$

In Fig.4 this ratio is plotted for different values of  $a_\vartheta/a_{x\xi}$ . For  $a_\vartheta/a_{x\xi} = 0.1$ , at the Nyquist limit we have a 1 to 10 Lagrangian-Smoothing ratio. At  $k_{\text{Nyquist}}/k_* = 4$  the split is even, while at  $k_{\text{Nyquist}}/k_* > 10$  the curve enters the Lagrangian dominated regime. This means that the noise-like grid scale oscillations will be strongly damped, while medium wavenumber Lagrangian motions will remain unchanged.

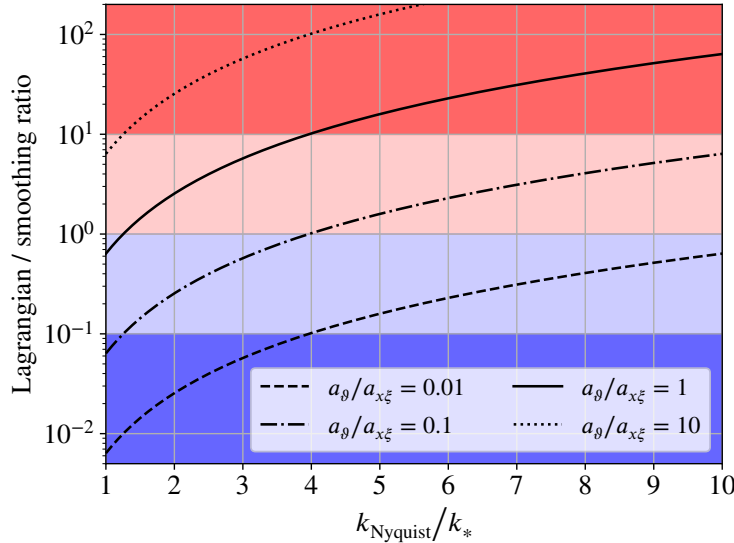


Figure 4: Diagrams of the Lagrangian-Smoothing ratio of eq.(31) based on the wavenumber for different values of  $a_g/a_{x\xi}$  at  $\omega_* = 2\pi$ . The y axis is in logarithmic scale. Lagrangian dominated areas are colored with red, while Smoothing dominated ones with blue.

As the  $a_g/a_{x\xi}$  ratio goes up, we see that this damping effect is reduced. With  $a_g/a_{x\xi} = 1$ , the split at the Nyquist wavenumber is even and the ratio quickly enters the Lagrangian regime. This is more apparent at  $a_g/a_{x\xi} = 10$  where at all wavenumbers the curve is essentially within the Lagrangian regime, while on the other hand the  $a_g/a_{x\xi} = 0.01$  curve is entirely on the below the Lagrangian regime for  $1 < k_{\text{Nyquist}}/k_* < 10$ .

From these observations, we see that the ratio  $a_g/a_{x\xi} = 0.1$  produces a balanced filter that smoothens grid-scale noise while also resolving the medium-sized motions. Values larger than this bias the solver toward Lagrangian dynamics and should be chosen carefully depending on the application. Ratios below 0.1 further suppress Lagrangian motion and are advisable in the case where rapid vertical mass transfer is essential, such as during wave breaking and overturning (see §5).

In summary, for cases with strong isopycnal deformation,  $a_g/a_{x\xi} \sim 0.01$  is advised, whereas  $a_g/a_{x\xi} \sim 0.1$  is preferable otherwise.

#### 4.5 Effect of the monitor function

Unlike the above analysis, when dealing with the case of  $a_M \neq 0$ , the elliptic equation has space-varying coefficients and thus we cannot utilize Fourier analysis. In order to better understand the monitor function term, we choose to study  $a_M$  alongside  $a_\xi$  with  $a_x = a_g = 0$ . Then, eq.(26) gives:

$$\frac{\partial}{\partial \xi} \left[ \left( 1 + \frac{a_M}{a_\xi} M^2 \right) \frac{\partial z}{\partial \xi} \right] = \frac{\partial^2 z_{ref}}{\partial \xi^2} \quad (32)$$

Integrating the above we get:

$$L = \frac{L_{ref} + C}{1 + A} \quad (33)$$

with  $A \stackrel{\text{def}}{=} \frac{a_M}{a_\xi} M^2$  and  $C$  a suitable integration constant.

If now we consider the reference configuration to almost be iso-spaced<sup>1</sup>, i.e.  $L_{ref}(x, \xi, t) \approx H(x, t)$  we get:

$$L = \frac{H}{1 + A} \left( \int_0^1 \frac{1}{1 + A} d\xi \right)^{-1} \quad (34)$$

<sup>1</sup>in the present paper, this assumption is exact, since the reference configuration is  $\sigma$ -grid

Thus, the ratio between the tallest and shortest cell is:

$$\frac{L_{\max}}{L_{\min}} = \frac{1 + \frac{a_M}{a_\xi} M_{\max}^2}{1 + \frac{a_M}{a_\xi} M_{\min}^2} \quad (35)$$

In all numerical examples that follow, in order to minimize the spurious numerical mixing (see §4.2) we chose the following monitor function, so that the RHS of eq.(21) is regulated:

$$M = \left| \frac{\partial \rho}{\partial \xi} \right| \Big/ \left| \frac{\partial \rho}{\partial \xi} \right|_{\max} \quad (36)$$

By doing this, the ratio  $a_M/a_\xi$  regulates the vertical cell size in areas with large density gradients. For example, according to eq.(35), if  $a_M/a_\xi = 1$ , areas where the density gradient is maximized will result in almost 2 times smaller cells than those where density is almost uniform, whereas the choice  $a_M/a_\xi = 2$  triples the mesh resolution in these areas.

That being said, high  $a_M/a_\xi$  ratios result in low numerical mixing, although excessively large values will deteriorate the overall quality since areas of constant density would become severely under-resolved. For the simulation of ISWs (which is the focus of the present paper), it was found through experimentation that  $a_M/a_{x\xi} = 10$  results in a balanced mesh resolution that greatly reduces SDM, as it will be demonstrated in §5.

#### 4.6 Numerical implementation of the variational minimizer

Having described the variational mesh movement, we now specify its implementation in the solver:

1. Calculate the horizontal GCL fluxes  $F_{i+1/2,j}^L$  through eq.(16a).
2. Based on this, use eq.(23) to get  $z_{lag}^*$  and specify the monitor function  $M(x, \xi)$ .
3. Solve the elliptic equation eq.(26) numerically on the  $x - \xi$  plane to calculate  $\vartheta_{i,j+1/2}$ .
4. Use these  $\vartheta_{i,j+1/2}$  to calculate the vertical numerical fluxes  $G_{i,j+1/2}$  through eq.(18).

An important feature of this approach is that it can be applied to any ocean model that is based on a GCL-type formulation. This is true for a large portion of ocean models, since the layers' heights are usually specified using the continuity equation. To adopt the proposed method, one can specify the Lagrangian impulse, the desired monitor function  $M$  and solve an elliptic problem without altering the structure of the solver.

With regards to the numerical cost, we note that the proposed procedure is an optional optimization. Consequently, the elliptic equation can be solved with moderate accuracy without significantly affecting the solver's overall performance. In the present study, we use the Jacobi iterative method with a finite differences space discretization on a classic 5-point orthogonal stencil. In this case, only a few number of iterations were found to be sufficient. More specifically, when using  $a_g = 0.1$ ,  $a_x = a_\xi = 1$ ,  $a_M = 10$ , only 3-7 iterations are needed when using the convergence threshold  $\|\mathbf{g}^{\text{previous}} - \mathbf{g}^{\text{next}}\|_\infty < 10^{-5}$ .

## 5 Results

In the following subsections, the ability of the proposed scheme to efficiently simulate stratified flows is demonstrated through various test cases of varying complexity. Specifically, in §5.2 the convergence of the solver towards an analytical ISW solution is presented. Following, in §5.3 and §5.4 the soliton-topography interaction of ISWs is investigated. Lastly, in §5.5 the breaking of an ISW over a sloping beach is investigated and comments are made with regard to the efficiency of the variational mesh movement strategy.

In all simulations, the timestep is calculated through the CFL condition found in [1] with a CFL constant of 0.45. At each test case, the results presented are mesh independent and produce stable solutions.

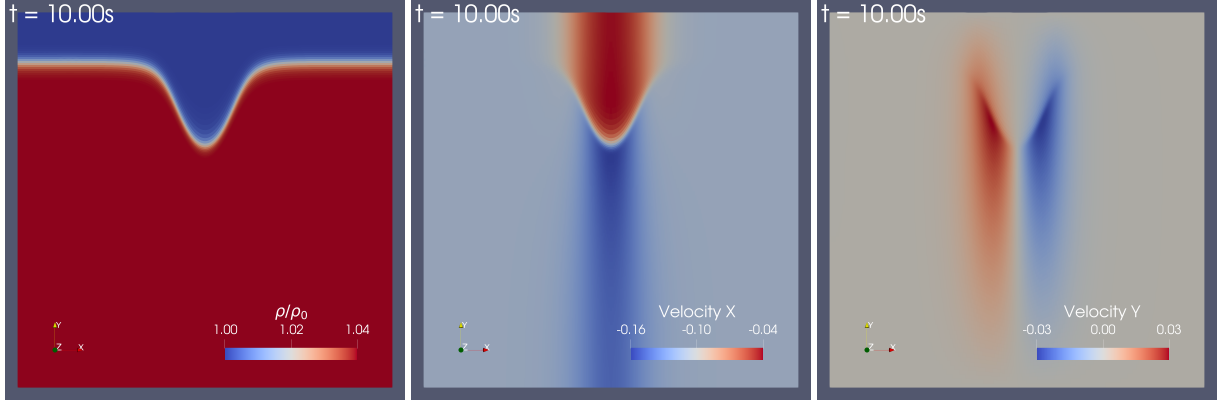
### 5.1 ISW generation

In the following, the Internal Solitary Waves (ISWs) are initialized using solutions of the Dubreil-Jacotin-Long (DJL) equation. Specifically, we utilize PyDJL<sup>2</sup> open source solver that employs the methodology described in [33] to nu-

<sup>2</sup><https://github.com/golnazir/PyDJL>

	$\rho_1 [kg/m^3]$	$\rho_2 [kg/m^3]$	depth[m]	$z_{pyc} [m]$	$h_{pyc} [mm]$	$APE [J]$	Amplitude[m]
§5.2 & §5.5	1000	1040	0.15	-0.02	2.50	$3.8000 \cdot 10^{-5}$	0.033
§5.3	990	1010	1.00	-0.25	8.75	$4.9335 \cdot 10^{-3}$	0.048
§5.4	996	1030	0.50	-0.10	40.00	$3.2700 \cdot 10^{-4}$	0.056

Table 1: Details of the ISWs used in the numerical test cases of §5.

Figure 5: Snapshot of the soliton of §5.2 (see Tab.1) at  $t = 10s$  on a  $1000 \times 100$  mesh. Contours of the normalized density, horizontal and vertical velocity are presented on a bounding box with the y axis being magnified with a factor of 10.

merically solve the DJL using Fourier expansions. In all cases, 4096 modes are used on each direction and the density profile is:

$$\rho(z) = \frac{\rho_1 + \rho_2}{2} - \frac{\rho_2 - \rho_1}{2} \tanh\left(\frac{z - z_{pyc}}{h_{pyc}}\right) \quad (37)$$

, with  $z_{pyc}$  and  $h_{pyc}$  being the location and thickness of the pycnocline. The soliton's amplitude is chosen by calibrating the Available Potential Energy (APE) that the code uses as input. Details about the ISWs for all benchmark cases considered herein are displayed in Table 1.

## 5.2 Convergence test on a traveling soliton

For the purpose of validating the solver's accuracy, a convergence test is conducted. Specifically, an ISW of amplitude  $0.033m$  (see Tab.1) on the domain  $(x, z) \in [0, 1.5] \times [0, -0.15]$  is used. At all boundaries, Dirichlet conditions are imposed:  $\mathbf{U} = \mathbf{U}_{th}$ , where  $\mathbf{U}_{th}$  is the analytical solution calculated at the boundary edges. The pressure obeys Neumann BC. Lastly, the solver uses the Boussinesq approximation (see §2).

In order to keep the soliton centered with respect to the computational domain, we subtract its traveling speed of  $c = 0.11279 m/s$  from the initial velocity field. By doing this, the soliton should remain fixed in the center of the frame and thus any deviation from the initial conditions is solely due to the numerical scheme. The solver is configured at isopycnal mode with  $\vartheta = 0$  and the simulation is terminated at  $t = 10s$ . To assess accuracy, the discrete  $L_2$  error norms of the velocity field are calculated:  $\|\mathbf{u}^n - \mathbf{u}^0\|_2 = \sqrt{\sum_{ij} (u_{ij}^n - u_{ij}^0)^2}$  with respect to the initial one  $\mathbf{u}^0$ . Various mesh sizes with  $n_x/n_l = 10$  are considered.

The flow field solution for a total  $1000 \times 100$  degrees of freedom (DOFs) is presented at Fig.5, while in Fig.6 the relative  $L^2$  error is plotted over DOFs. It is evident that the solver converges to the analytic solution with second order accuracy that is only reduced to first order at large DOFs, at about  $10^5$ .

These error curves show that the solver converges in a robust way, while staying below the relative error of 1% even at a small number of DOFs. Thus, we conclude that SLS can accurately model the propagation of ISWs and its use on the test cases that follow is highly justified.

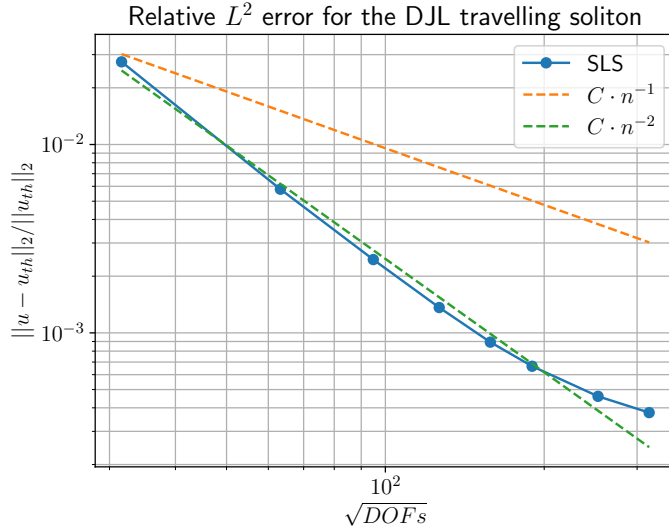


Figure 6: Convergence of the  $L^2$  error norm of the velocity with respect to the square root of the total Degrees of Freedoms (DOFs). The error is normalized using norm of the initial velocity field. First and second order ideal curves are presented in dashed lines. Both axes are logarithmic.

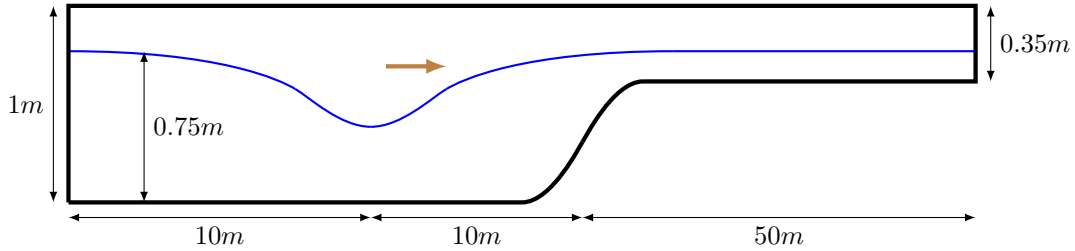


Figure 7: Sketch of the ISW shoaling test case of §5.3. The ISW data can be seen in Tab.1, while the topography is defined by eq.(38). The ISW propagates rightwards, while all boundaries are considered as impermeable walls.

### 5.3 Shoaling of an ISW on a shelf

Next, we consider the shoaling of an ISW by considering the s8c1c test case of [34]. The data of the soliton is again detailed in Tab.1, while the configuration of the domain can be seen in Fig.7. The topography changes with a maximum slope of 1/10 at  $x = 0$  through the following relation taken from [34]:

$$h(x) = 1 - \frac{2.5}{10} \left[ \text{inttanh} \left( \frac{x + 3.25}{2.5} \right) - \text{inttanh} \left( \frac{x - 3.25}{2.5} \right) \right] \quad (38)$$

with  $\text{inttanh}(x) \stackrel{\text{def}}{=} \int_{-\infty}^x \tanh(x) dx = x + \ln(2 \cosh x)$

For the simulation, a mesh of  $19200 \times 32$  cells is used and  $a_\theta = 0.1$ ,  $a_x = a_\xi = 1$  and  $a_M = 10$  are considered alongside the Boussinesq approximation (see §2). On all boundaries, inviscid wall BCs are imposed. Snapshots of SLS's results alongside those of [34] are presented in Fig.8.

From an observational standpoint, the soliton propagates without breaking, but it is subject to strong bottom-induced dispersion that generates a wavetrain containing more than 10 distinct wave crests. Since dispersion is inherently nonhydrostatic, such phenomena necessitate a careful treatment of the nonhydrostatic pressure, as the one presented herein.

In Fig.8, the density field contour from the SLS results is presented side-by-side with those of [34] at various timestamps. The contours have the same scale and bounding boxes with the [34] ones and the comparison between them indicates no noticeable differences. This observed agreement further validates SLS in this challenging case, since dispersive phenomena of this nature necessitate a good combined resolution of multiple harmonics at different frequencies.

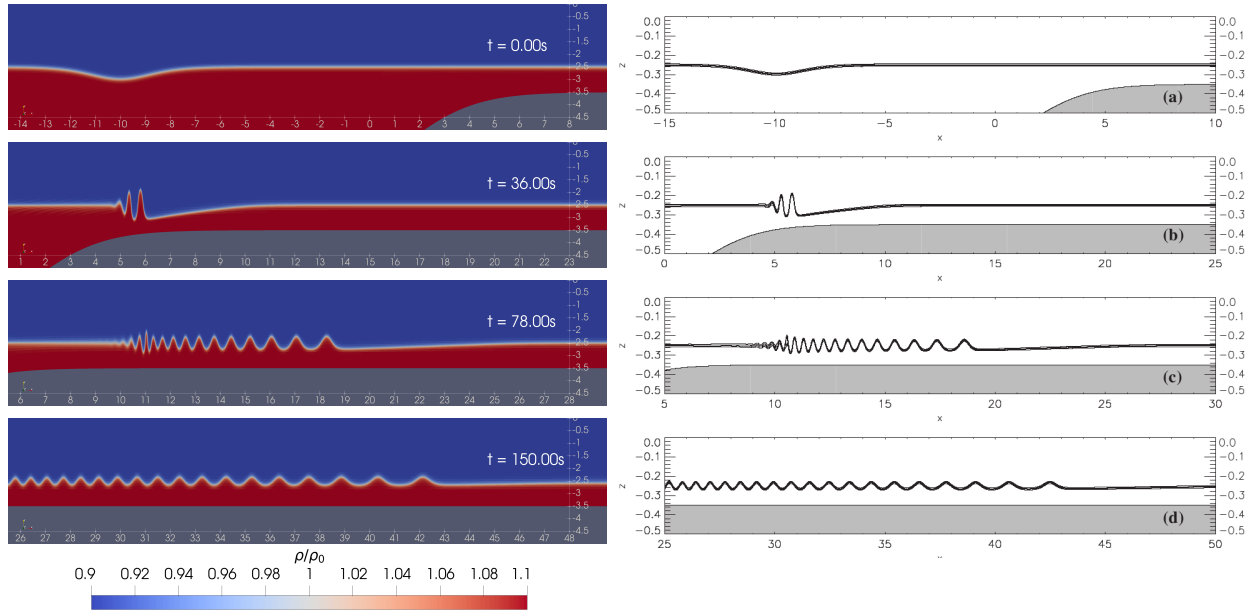


Figure 8: Snapshots of density contours at various timestamps for the shoaling ISW of §5.3. On the left are the SLS results and on the right, those from [34]. In the SLS contours, the y axis is magnified by a factor of 10 for better readability.

With respect to the ALE movement, its performance is robust and no serious SDM appears. This indicates a good performance in ISW propagation phenomena, when no excessive isopycnal deformation occurs, while its robustness in more demanding configurations is assessed below.

#### 5.4 ISW interaction with a submerged wedge

To further investigate soliton-topography interactions, we focus on the interaction of an ISW with a submerged obstacle. Specifically, we consider the experiments of [35], where a submerged wedge with  $45^\circ$  angle and height of  $0.3m$  is placed at  $x = 0$ . The depth of the tank is  $0.5m$  and the data of the soliton can be found in Tab.1.

According to the experiments, the ISW is expected to impact the wedge in a violent manner and then to continue and propagate past it. In order to properly capture this numerically, the solver must be able to sharply capture the ISW without severe numerical diffusion/mixing, while retaining a robust mesh quality during the impact upon the obstacle. This produces a challenge, that if properly addressed will further solidify the validity of the proposed method.

A mesh of total  $2000 \times 30$  cells is employed that covers the domain  $(x, z) \in [-6, 4] \times [-0.5, 0]$ . Again, SLS uses the variational mesh movement  $a_x = a_\xi = 1$  and  $a_M = 10$ . Since the impact on the wedge heavily distorts the isopycnals, the value  $a_g = 0.01$  is utilized based on the discussion of §4.4. All boundaries are considered impenetrable walls except the top one, where a zero pressure free-surface condition is enforced.

In Fig.9, density contours over the computational mesh are presented at various time values, just left to the obstacle during the impact of the ISW upon it. Regarding the mesh movement algorithm, we observe that indeed with  $a_M = 10$  and  $a_\xi = 1$  areas with large density gradients have almost 10 times bigger vertical resolution compared to the constant density regions, thus resulting in a sharp pycnocline tracking. We also observe that the algorithm correctly triggers vertical mass transfer when the isopycnals tend to distort and overturn at the point where the ISW impacts on the wedge. The result is a smooth mesh that concentrates the mesh in areas where the production of SDM would otherwise be large. A moderate amount of mixing is noticed at the point of overturning when vertical advection is triggered, but it is generally moderate and doesn't severely pollute the solution. When the ISW passes above the wedge, the mesh progressively returns to its original configuration.

To assess the results, in Fig.10, where the timeseries of the pycnocline's center elevation at various locations throughout the domain is compared with the experimental measurements of [35]. The pycnocline center is defined as the location of the point of where the density is equal to  $(\rho_{\min} + \rho_{\max})/2$ . The comparison between the SLS and the experiments is generally good. Some discrepancies exist at the  $x = -3m$  probe, where some wiggles that SLS doesn't capture appear

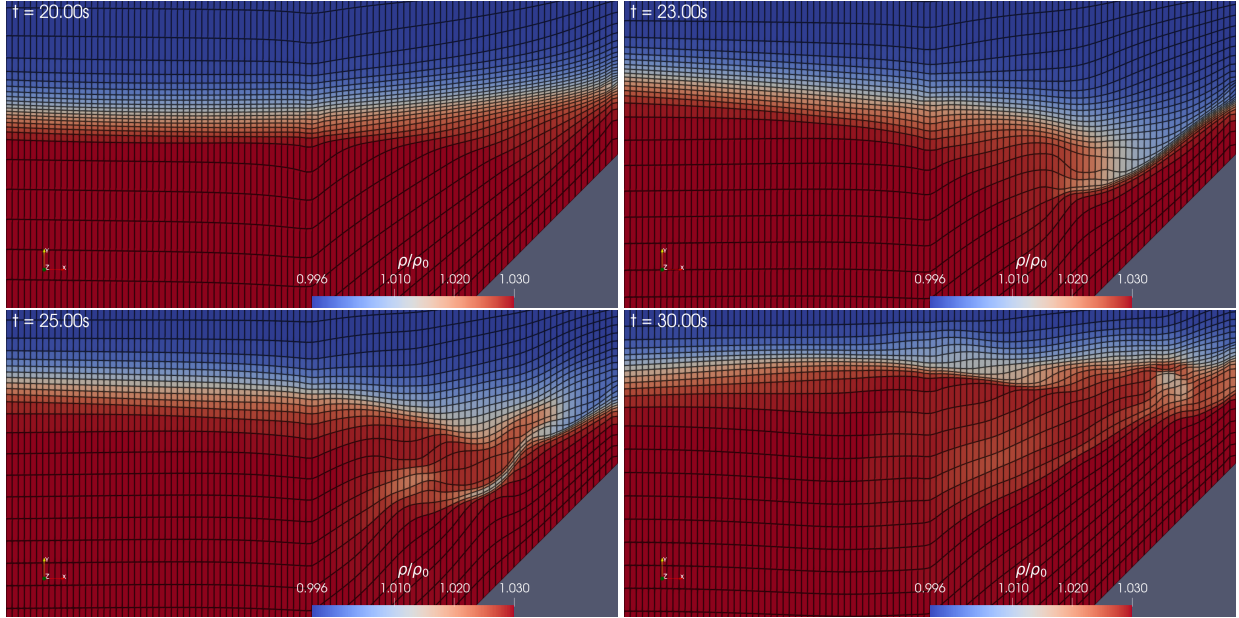


Figure 9: Density contours of the ISW propagating and impacting on the submerged wedge at  $t[s] = \{20, 23, 25, 30\}$  alongside the computational mesh.

in the experiments. These wiggles are attributed to the ISW generation in the experimental setup, in which a sliding gate is used which maybe created some trailing secondary waves. This is further reinforced by the fact that in [36] where (like here) the DJL equation is used to initialize this configuration, those wiggles are also absent. That being said, the SLS results seem to be in agreement with the experiments, thus further validating the ability of the solver to simulate nonhydrostatic ISW-topography interactions.

### 5.5 ISW breaking on a sloping beach

The last test case investigates the effectiveness of the proposed variational mesh movement on a complex phenomenon that includes overturning of the isopycnal surfaces and thus more nuanced approaches must be considered. Thus, we focus on the breaking of an ISW on a linear and emerging beach-like topography. The subject of the breaking of ISWs has been the subject of numerous studies, due to the complexity of the phenomenon and its critical role in the continental shelf cascade of energy that it triggers. For an extensive review of the subject, the reader is referred to [17].

Unlike the previous ones, in this test case a purely isopycnal formulation would totally fail to capture the phenomenon since such a scheme negates vertical mass transfer that is an inherent feature of wave breaking. As such, it is natural to assume that overly limiting  $\vartheta$  through a large Lagrangian bias ( $a_\vartheta$ ) would produce erroneous results. Thus, in order to reduce spurious mixing, one should consider the use of the  $a_M$  parameter so that the vertical spacing is denser at areas with large vertical density gradients. The results that follow will demonstrate the effectiveness of this approach.

Specifically, we consider case 60 from [37], where an ISW with the same characteristics as the one in §5.2 propagates towards a beach with constant slope equal to 0.3. The phenomenon consists of a plunging breaker and thus overturning and vertical mixing is prevalent.

The numerical domain consists of  $600 \times 75$  cells that cover the area  $(x, z) \in [0, 3] \times [-0.15, 0]$ , while the bottom starts to slope upwards at  $x = 2.4m$ . All boundaries are considered as impenetrable walls. At all cases, the Boussinesq approximation is used (see §2). The variational mesh movement is utilized with  $a_x = a_\xi = 1$ , with  $a_\vartheta, a_M$  varying between simulations. A simulation on a fixed  $\sigma$ -grid is also performed by prescribing  $\vartheta$  through [1, eq.(16b)].

In order to properly quantify spurious numerical mixing of the density, at each timestep we calculate the discrete second order moment of the density  $\iiint \rho^2 dV \approx I \stackrel{\text{def}}{=} \sum (\rho_{ij})^2 L_{ij} \Delta x_i \Delta \xi_j$ . The rate of decay of  $I$  will indicate the amount of numerical diffusion that the solver introduces (see the discussion in §4.2). In Fig.11, the times series of the relative deviation  $\frac{I(t) - I(t=0)}{I(t=0)}$  are presented for various values of  $(a_\vartheta, a_M)$ . Specifically, we use  $a_\vartheta = 0.01$  and  $a_M = 0$  as a baseline configuration and try to see how SDM behaves by increasing one or both of them.

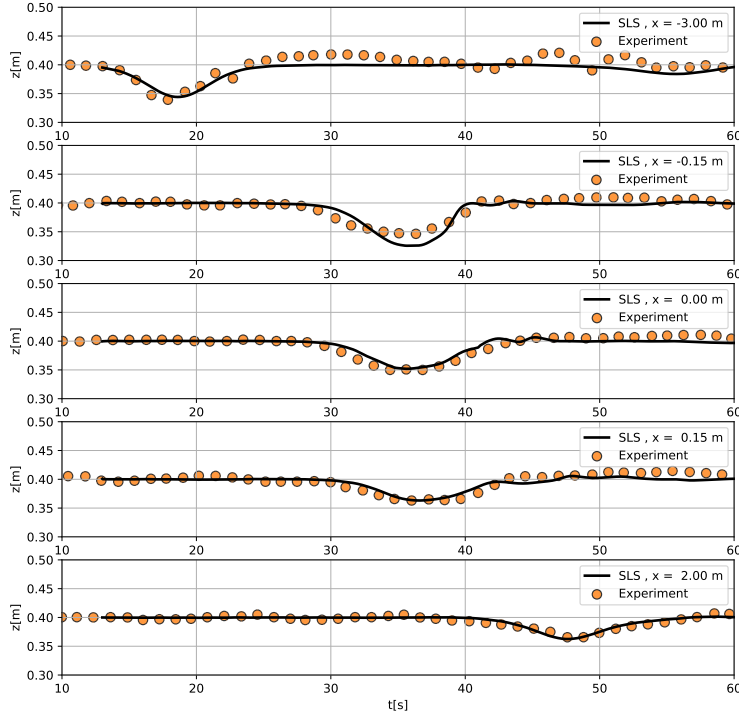


Figure 10: Timeseries of the pycnocline vertical location at various locations throughout the domain for the case of ISW propagating above a submerged wedge. SLS results are presented with continuous lines, while experimental measurements from [35] are noted with circles.

In this baseline configuration, the effect of the numerical mixing in the results is apparent. Even before the ISW reaches the slope, heavy numerical diffusion is observed in Fig.12 at the point where the pycnocline intersects the topography. Also, numerical mixing is observed at the ISW at the left side of its crest. This diffusive behavior of the  $(a_g, a_M) = (0.01, 0)$  configuration is also displayed in Fig.11, where the decay of  $I$  is almost linear up to the point of breaking ( $t \approx 18s$ ) and almost identical with the  $\sigma$ -grid configuration.

In order to counteract this, we could introduce Lagrangian bias through  $a_g$  and keeping  $a_M = 0$ . From Fig.11, we see that as  $a_g$  increases, the decay of  $I$  is reduced. But, as we see in Fig.14, when using large values ( $a_g = 1$ ) vertical mass transfer is suppressed in an highly nonphysical manner and the results do not capture the overturning correctly.

Because of this, if we want to further diminish numerical mixing, we must also employ the monitor function strategy through  $a_M$ . Indeed, we see that by using  $a_g = 0.01$ , values of  $a_M$  between 1 and 10 seem to greatly reduce numerical mixing up until to the point that the ISW starts to break. After the point of overturning ( $t > 18s$ ), numerical mixing is mainly the result of the horizontal advection scheme that a vertical ALE method cannot reduce. Indeed, by comparing Fig.12 and Fig.13, we see that the latter displays a much clearer result that greatly improves the resolution around the density interface.

Summarizing the above observations, we conclude that when vertical mass transfer is important, it is advisable to keep  $a_g$  at a moderate value  $a_g \sim 0.01$  and try to reduce SDM through  $a_M$ . Indeed, the pair  $(a_g, a_M) = (0.01, 10)$ , as demonstrated in Fig.11, almost negates the decay of  $\iiint \rho^2 dV$  and simultaneously captures the overturning accurately (Fig.13).

With regards to the phenomenon, the results of SLS closely resemble those of [37]: When the ISW approaches the slope, its crest steepens, until the critical point of overturning, when a mass of light water enters the dense region, while the dense front propagates to the right. Afterwards, mixing occurs and a portion of the ISW is reflected leftwards. The above results indicate the ability of SLS to simulate nonhydrostatic flows of complex nature. Furthermore, through the proposed mesh moving formulation, SLS is able to have a low level of numerical dissipation without overly suppressing the physically relevant mass transfer.

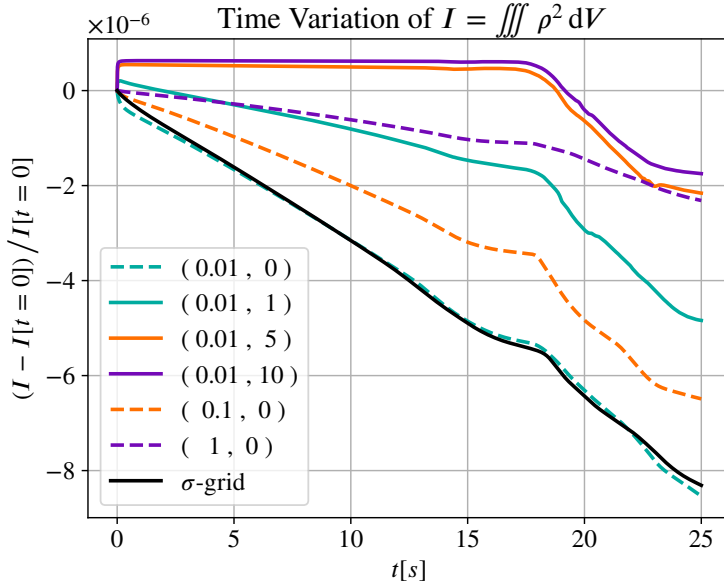


Figure 11: Decay of the relative second order moment of the density field for the case of plunging breaker in §5.5. In the legend, the two numbers indicate the values of the parameters  $(a_g, a_M)$

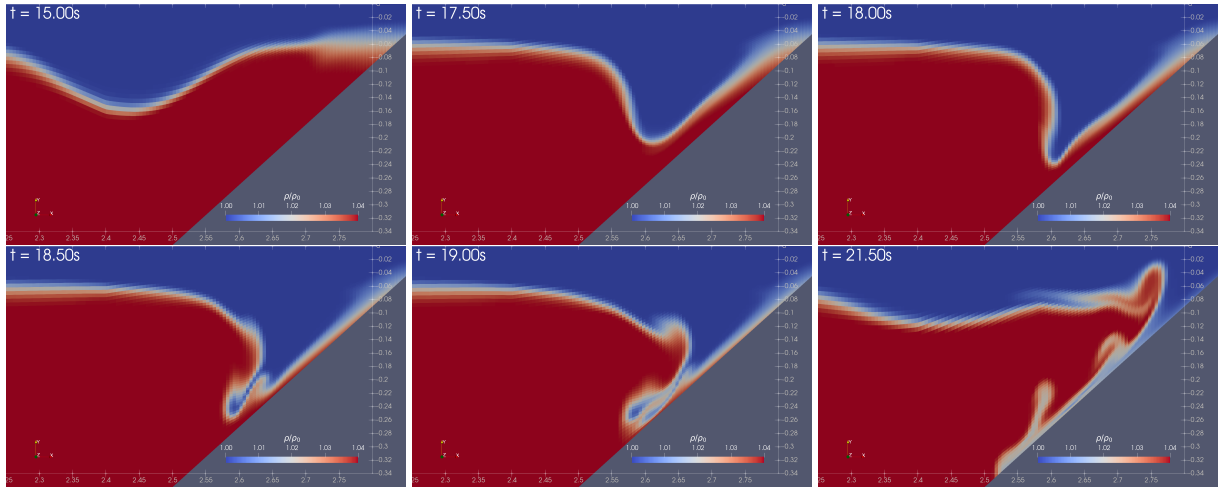


Figure 12: ISW plunging into a sloping beach, normalized density contours from SLS simulation with  $(a_g, a_M) = (0.01, 0)$ . The vertical axis and its labels are magnified by a factor of 3 and the dimensional time value is noted at each frame.

## 6 Concluding remarks

In the present paper, a ALE vertical mesh movement strategy was applied to a nonhydrostatic ocean model. The mesh movement is defined through the minimization of eq.(25) that results in the elliptic equation of eq.(26). The cost functional includes various target objectives that are weighted by user-defined coefficients. These goals include a Lagrangian tendency and a monitor function that increases the vertical mesh resolution in areas of interest, accompanied by smoothing towards a reference configuration. Those coefficients were analyzed in §4.4,4.5 and some guidelines were laid out.

In §5, the numerical scheme alongside the mesh movement were validated: In §5.2 the second order convergence of the solver towards an analytical ISW solution was verified. Afterwards, the shoaling ISW on a tanh-like bottom in §5.3 alongside the interaction of an ISW with a submerged obstacle in §5.4 were considered. The ability of SLS

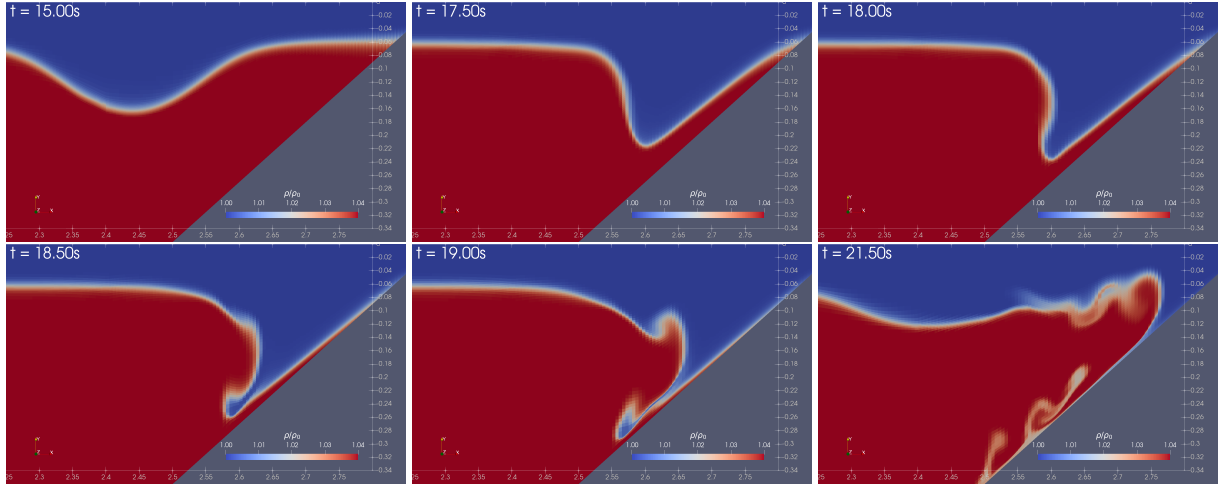


Figure 13: ISW plunging into a sloping beach, normalized density contours from SLS simulation with  $(a_g, a_M) = (0.01, 10)$ . The vertical axis and its labels are magnified by a factor of 3 and the dimensional time value is noted at each frame.

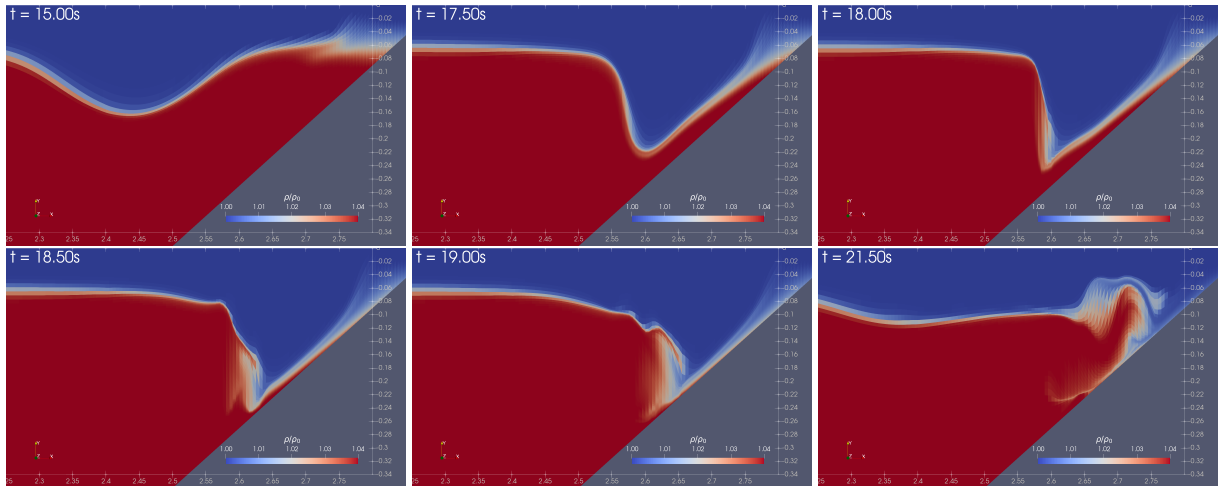


Figure 14: ISW plunging into a sloping beach, normalized density contours from SLS simulation with  $(a_g, a_M) = (1, 0)$ . The vertical axis and its labels are magnified by a factor of 3 and the dimensional time value is noted at each frame.

to accurately simulate those phenomena with fidelity indicates its applicability in nonhydrostatic stratified flows and further reinforces its validity in simulating oceanographic phenomena of interest.

Lastly, the effect of the variational mesh movement in mitigating SDM is thoroughly investigated in §5.5 for the demanding case of ISW breaking. Various values of the cost functional coefficients were tested and SDM was quantified through the second moment of density  $\iiint \rho^2 dV$ . The results indicate that although numerical mixing can be severely reduced by the Lagrangian bias, an excessive value of the corresponding coefficient might result in suppression of physically relevant vertical mass transfer. On the other hand, keeping the Lagrangian bias at the mild value ( $a_g \sim 0.01$ ) and using a monitor function that increases resolution in areas with large density gradients, one can achieve significant reduction in numerical mixing without producing nonphysical results as indicated in Fig.11.

Concluding, the proposed variational mesh movement successfully reduces spurious numerical mixing through a formulation that is both compact and easy to implement. Furthermore, due to the versatile nature of the mathematical formulation, adding additional target goals in the optimization process is quite straightforward. As a next step, the application of this methodology will be investigated in flows of larger spatiotemporal scales, where additional optimality criteria could perhaps be needed.

## Acknowledgments

The research work was supported by the Greek State Scholarship Foundation (IKY) under the Chrysovergis grant. The first author is the recipient for the 2024 scholarship in the domain of Physics that fully funds his PhD studies at NTUA and gratefully acknowledges this financial support. The authors also extend their gratitude to S. Zafeiris for his constructive comments that helped improve the quality of the manuscript.

## References

- [1] Andreas Alexandris-Galanopoulos, George Papadakis, and Kostas Belibassakis. A semi-lagrangian splitting framework for the simulation of non-hydrostatic free-surface flows. *Ocean Modelling*, 187:102290, 2024.
- [2] Baylor Fox-Kemper, Alistair Adcroft, Claus W Böning, Eric P Chassignet, Enrique Curchitser, Gokhan Danabasoglu, Carsten Eden, Matthew H England, Rüdiger Gerdes, Richard J Greatbatch, et al. Challenges and prospects in ocean circulation models. *Frontiers in Marine Science*, 6:65, 2019.
- [3] Stephen M Griffies, Claus Böning, Frank O Bryan, Eric P Chassignet, Rüdiger Gerdes, Hiroyasu Hasumi, Anthony Hirst, Anne-Marie Treguier, and David Webb. Developments in ocean climate modelling. *Ocean Modelling*, 2(3-4):123–192, 2000.
- [4] Victor P Starr. A quasi-lagrangian system of hydrodynamical equations. *Journal of the Atmospheric Sciences*, 2(4):227–237, 1945.
- [5] Rainer Bleck. An oceanic general circulation model framed in hybrid isopycnic-cartesian coordinates. *Ocean modelling*, 4(1):55–88, 2002.
- [6] Eric P Chassignet, Harley E Hurlbert, Ole Martin Smedstad, George R Halliwell, Patrick J Hogan, Alan J Wallcraft, Remy Baraille, and Rainer Bleck. The hycom (hybrid coordinate ocean model) data assimilative system. *Journal of Marine Systems*, 65(1-4):60–83, 2007.
- [7] Alistair Adcroft, Whit Anderson, V Balaji, Chris Blanton, Mitchell Bushuk, Carolina O Dufour, John P Dunne, Stephen M Griffies, Robert Hallberg, Matthew J Harrison, et al. The gfdl global ocean and sea ice model om4. 0: Model description and simulation features. *Journal of Advances in Modeling Earth Systems*, 11(10):3167–3211, 2019.
- [8] Tal Ezer and George L Mellor. A generalized coordinate ocean model and a comparison of the bottom boundary layer dynamics in terrain-following and in z-level grids. *Ocean Modelling*, 6(3-4):379–403, 2004.
- [9] Ronald C Pacanowski, K Dixon, and Anthony Rosati. The gfdl modular ocean model users guide. *GFDL Ocean Group Tech. Rep.*, 2:142, 1991.
- [10] Alan F Blumberg and George L Mellor. A description of a three-dimensional coastal ocean circulation model. *Three-dimensional coastal ocean models*, 4:1–16, 1987.
- [11] Stephen M Griffies, Alistair Adcroft, and Robert W Hallberg. A primer on the vertical lagrangian-remap method in ocean models based on finite volume generalized vertical coordinates. *Journal of Advances in Modeling Earth Systems*, 12(10):e2019MS001954, 2020.
- [12] Matthieu Leclair and Gurvan Madec. z-coordinate, an arbitrary lagrangian–eulerian coordinate separating high and low frequency motions. *Ocean Modelling*, 37(3-4):139–152, 2011.
- [13] Mark R Petersen, Douglas W Jacobson, Todd D Ringler, Matthew W Hecht, and Mathew E Maltrud. Evaluation of the arbitrary lagrangian–eulerian vertical coordinate method in the mpas-ocean model. *Ocean Modelling*, 86:93–113, 2015.
- [14] Hans Burchard and Jean-Marie Beckers. Non-uniform adaptive vertical grids in one-dimensional numerical ocean models. *Ocean Modelling*, 6(1):51–81, 2004.
- [15] Hans Burchard and Hannes Rennau. Comparative quantification of physically and numerically induced mixing in ocean models. *Ocean modelling*, 20(3):293–311, 2008.
- [16] Richard Hofmeister, Hans Burchard, and Jean-Marie Beckers. Non-uniform adaptive vertical grids for 3d numerical ocean models. *Ocean Modelling*, 33(1-2):70–86, 2010.
- [17] Marek Stastna and Sierra Legare. Simulations of shoaling large-amplitude internal waves: perspectives and outlook. *Flow*, 4:E11, 2024.
- [18] JJIM Van Kan. A second-order accurate pressure-correction scheme for viscous incompressible flow. *SIAM journal on scientific and statistical computing*, 7(3):870–891, 1986.
- [19] Bram Van Leer. Towards the ultimate conservative difference scheme. v. a second-order sequel to godunov’s method. *Journal of computational Physics*, 32(1):101–136, 1979.
- [20] Philip L Roe. Some contributions to the modelling of discontinuous flows. *Large-scale computations in fluid mechanics*, pages 163–193, 1985.
- [21] Andreas Alexandris-Galanopoulos and George Papadakis. Development of a semi-lagrangian-splitting ocean model: Extension to abrupt bathymetries and wave-structure interactions. In *International Congress of the International Maritime Association of the Mediterranean*, pages 338–350. Springer, 2025.

- [22] Andreas Bollermann, Guoxian Chen, Alexander Kurganov, and Sebastian Noelle. A well-balanced reconstruction of wet/dry fronts for the shallow water equations. *Journal of Scientific Computing*, 56:267–290, 2013.
- [23] Emmanuel Audusse, Fran ois Bouchut, Marie-Odile Bristeau, Rupert Klein, and Beno t Perthame. A fast and stable well-balanced scheme with hydrostatic reconstruction for shallow water flows. *SIAM Journal on Scientific Computing*, 25(6):2050–2065, 2004.
- [24] Alexander Kurganov. Finite-volume schemes for shallow-water equations. *Acta Numerica*, 27:289–351, 2018.
- [25] Patrick Ersing, Sven Goldberg, and Andrew R Winters. Entropy stable hydrostatic reconstruction schemes for shallow water systems. *Journal of Computational Physics*, 527:113802, 2025.
- [26] Eitan Tadmor. The numerical viscosity of entropy stable schemes for systems of conservation laws. i. *Mathematics of Computation*, 49(179):91–103, 1987.
- [27] Edward S Gross, Luca Bonaventura, and Giorgio Rosatti. Consistency with continuity in conservative advection schemes for free-surface models. *International Journal for Numerical Methods in Fluids*, 38(4):307–327, 2002.
- [28] Xin Liu, Jason Albright, Yekaterina Epshteyn, and Alexander Kurganov. Well-balanced positivity preserving central-upwind scheme with a novel wet/dry reconstruction on triangular grids for the saint-venant system. *Journal of Computational Physics*, 374:213–236, 2018.
- [29] Philippe Delandmeter, Jonathan Lambrechts, Vincent Legat, Valentin Vallaeys, Jaya Naithani, Wim Thiery, Jean-Fran ois Remacle, and Eric Deleersnijder. A fully consistent and conservative vertically adaptive coordinate system for slim 3d v0. 4 with an application to the thermocline oscillations of lake tanganyika. *Geoscientific Model Development*, 11(3):1161–1179, 2018.
- [30] Tridib Banerjee, Sergey Danilov, Knut Klingbeil, and Jean-Michel Campin. Discrete variance decay analysis of spurious mixing. *Ocean Modelling*, 192:102460, 2024.
- [31] Weiming Cao, Weizhang Huang, and Robert D Russell. A study of monitor functions for two-dimensional adaptive mesh generation. *SIAM Journal on Scientific Computing*, 20(6):1978–1994, 1999.
- [32] Weizhang Huang and Weiwei Sun. Variational mesh adaptation ii: error estimates and monitor functions. *Journal of computational physics*, 184(2):619–648, 2003.
- [33] M. Dunphy, C. Subich, and M. Stastna. Spectral methods for internal waves: indistinguishable density profiles and double-humped solitary waves. *Nonlinear Processes in Geophysics*, 18(3):351–358, 2011.
- [34] Kevin G Lamb and Wenting Xiao. Internal solitary waves shoaling onto a shelf: Comparisons of weakly-nonlinear and fully nonlinear models for hyperbolic-tangent stratifications. *Ocean Modelling*, 78:17–34, 2014.
- [35] Chih-Min Hsieh, Robert R Hwang, John R-C Hsu, and Ming-Hung Cheng. Numerical modeling of flow evolution for an internal solitary wave propagating over a submerged ridge. *Wave Motion*, 55:48–72, 2015.
- [36] Jingyuan Li, Qinghe Zhang, and Tongqing Chen. Iswofoam: A numerical model for internal solitary wave simulation in continuously stratified fluids. *Geoscientific Model Development*, 15(1):105–127, 2022.
- [37] Payam Aghsaei, Leon Boegman, and Kevin G Lamb. Breaking of shoaling internal solitary waves. *Journal of Fluid Mechanics*, 659:289–317, 2010.
- [38] Izrail Moiseevitch Gelfand, Richard A Silverman, et al. *Calculus of variations*. Courier Corporation, 2000.

## A Finite Element formulation of pressure correction

Let us consider test functions  $N \in \mathcal{H}_{0,f_s}^1$  that have zero trace at the free-surface and multiply eq.(8b) with them:

$$\iiint_D N \operatorname{div}(\mathbf{V}^{n+1}) \, dV = 0 \iff \iiint_D \mathbf{V}^{n+1} \cdot \mathbf{grad} N \, dV = \iiint_D \operatorname{div}(\mathbf{V}^{n+1} N) \, dV \quad (39)$$

By applying the Green-Gauss theorem and considering the Neumann boundary conditions  $\mathbf{V}^{n+1} \cdot \mathbf{n} = v_{bc}$  on  $\partial\mathcal{D}_N = \partial\mathcal{D} \setminus \partial\mathcal{D}_{f_s}$  we get:

$$\iiint_D [\mathbf{V}^{n+1} \cdot \mathbf{grad} N] \, dV = \iint_{\partial\mathcal{D}_N} v_{bc} N \, dS \quad (40)$$

Inserting eq.(8a) with  $\phi \stackrel{\text{def}}{=} \Delta t(q^{n+1} - q^n)$  into eq.(40) we get:

$$\iiint_D \frac{1}{\rho^*} (\mathbf{grad} \phi) \cdot (\mathbf{grad} N) \, dV = \iiint_D \mathbf{V}^* \cdot (\mathbf{grad} N) \, dV - \iint_{\partial\mathcal{D}_N} v_{bc} N \, dS \quad (41)$$

Thus the weak formulation of eq.(8) is to find  $\phi \in \mathcal{H}_{0,f_s}^1$  so that eq.(41) holds for every  $N \in \mathcal{H}_{0,f_s}^1$ .

Now, we proceed to the definition of the various matrices. Inside a cell  $\Omega_{ij}$  the Q4 elements have the following local parametric shape functions:

$$N^{(1)} = ts \quad (42a)$$

$$N^{(2)} = (1-t)s \quad (42b)$$

$$N^{(3)} = t(1-s) \quad (42c)$$

$$N^{(4)} = (1-t)(1-s) \quad (42d)$$

with  $s = \frac{x - x_i}{\Delta x_i}$  and  $t = \frac{\xi - \xi_j}{\Delta \xi_j}$

Using these local shape functions, to discretize eq.(41), we need to calculate their gradients on the physical space. Thus, inside a cell  $\Omega_{km}$  we approximate the gradient of  $N_{ij}$  using:

$$\mathbf{grad} N_{ij} \Big|_{\Omega_{km}} \approx \begin{bmatrix} \frac{\partial N_{ij}}{\partial x} - \frac{\overline{(Z_x)}_{km}}{L_{km}} \frac{\partial N_{ij}}{\partial \xi} \\ \frac{1}{L_{km}} \frac{\partial N_{ij}}{\partial \xi} \end{bmatrix} \quad (43)$$

with  $(Z_x)_{ij} = \frac{z_{i+1,j} - z_{i,j}}{(\Delta x_{i+1} + \Delta x_i)/2}$  and  $\overline{(Z_x)}_{km} = \frac{(Z_x)_{ij} + (Z_x)_{i+1,j} + (Z_x)_{i,j+1} + (Z_x)_{i+1,j+1}}{4}$  being the nodal and cell-averaged gradients respectively.

By doing so, the gradients inside  $\Omega_{ij}$  are polynomial and can be integrated analytically.

If now we insert the expansion  $q_h \approx \sum q_k N_k$  into eq.(41) we get:

$$\sum_{m \in \text{nodes}} \iiint_D \frac{1}{\rho^*} (\mathbf{grad} N_m \cdot \mathbf{grad} N_k) \phi_m \, dV = \iiint_D \mathbf{V}^* \cdot \mathbf{grad} N_k \, dV - \iint_{\partial D_N} N_k v_{bc} \, dS \quad (44)$$

In the above eq. and below, we substitute  $(i, j)$  into single index notation with  $k, m, l$ .

Since  $\mathbf{V}, \rho$  come from the FV discretization, they are constant within each cell  $\Omega_k$ , we can compute:

$$\{K\}_{km} \stackrel{\text{def}}{=} \sum_{l \in \text{cells}} \frac{1}{\rho_l^*} \iiint_{\Omega_l} \mathbf{grad} N_k \mathbf{grad} N_m \, dV \quad (45a)$$

$$\iiint \mathbf{V}^* \cdot \mathbf{grad} N_k \, dV = \sum_{l \in \text{cells}} \mathbf{V}_l^* \cdot \iiint_{\Omega_l} \mathbf{grad} N_k \, dV \stackrel{\text{def}}{=} \sum_{l \in \text{cells}} (G_{kl}^x u_l^* + G_{kl}^z w_l^*) \quad (45b)$$

$$\iint_{\partial D_N} N_k v_{bc} \, dS = \sum_{l \in \text{boundary faces}} (v_{bc})_l \iint_{(\partial D)_l} N_k \, dS \stackrel{\text{def}}{=} \sum_{l \in \text{boundary faces}} B_{kl} (v_{bc})_l \quad (45c)$$

## B Discrete Variance Decay

We present the discrete variance decay (see [30]) of the vertical advection scheme using the space semi-discrete scheme (the  $i$  index is dropped for readability):

$$\Delta \xi_j \frac{\partial L_j}{\partial t} + \vartheta_{j+1} - \vartheta_j = 0 \quad (46)$$

$$\Delta \xi_j \frac{\partial}{\partial t} (L_j \rho_j) + (\vartheta \rho)_{j+1/2} - (\vartheta \rho)_{j-1/2} = 0 \quad (47)$$

where the fluxes due to the upwinding of eq.(18) can be written alternatively for the zero order reconstruction (piecewise constant per cell) case as:

$$(\vartheta \rho)_{j+1/2} = \vartheta_{j+1/2} \frac{\rho_{j+1} + \rho_j}{2} - \frac{|\vartheta_{j+1/2}|}{2} (\rho_{j+1} - \rho_j) \quad (48)$$

Then, we can calculate the discrete variance:

$$\begin{aligned} \frac{1}{2} \Delta\xi_j \frac{\partial}{\partial t} (L_j \rho_j^2) &= \Delta\xi_j \left[ \rho_j \frac{\partial}{\partial t} (L_j \rho_j) - \frac{\rho_j^2}{2} \frac{\partial L_j}{\partial t} \right] \Rightarrow \\ \Rightarrow \frac{1}{2} \Delta\xi_j \frac{\partial}{\partial t} (L_j \rho_j^2) + \rho_j &\left[ (\vartheta\rho)_{j+1/2} - (\vartheta\rho)_{j-1/2} \right] - \frac{\rho_j^2}{2} [\vartheta_{j+1} - \vartheta_j] = 0 \end{aligned} \quad (49)$$

by substituting the fluxes and using the identity:

$$\rho_j(\rho_{j+1} - \rho_j) = \left( \rho_j + \frac{\rho_{j+1} - \rho_j}{2} - \frac{\rho_{j+1} - \rho_j}{2} \right) (\rho_{j+1} - \rho_j) = \frac{\rho_{j+1} + \rho_j}{2} (\rho_{j+1} - \rho_j) - \frac{1}{2} (\rho_{j+1} - \rho_j)^2 \quad (50)$$

we arrive at the following evolution equation:

$$\frac{1}{2} \Delta\xi_j \frac{\partial}{\partial t} (L_j \rho_j^2) + F_{j+1/2}^{en} - F_{j-1/2}^{en} = -\frac{1}{4} |\vartheta_{j+1/2}| (\rho_{j+1} - \rho_j)^2 - \frac{1}{4} |\vartheta_{j-1/2}| (\rho_j - \rho_{j-1})^2 \quad (51)$$

with  $F_{j+1/2}^{en} \stackrel{\text{def}}{=} \vartheta_{j+1/2} \frac{\rho_j \rho_{j+1}}{2} - \frac{1}{4} |\vartheta_{j+1/2}| (\rho_{j+1} + \rho_j)(\rho_{j+1} - \rho_j)$ . If, now, we sum over  $j$  we have:

$$\frac{d}{dt} \sum_{j=1}^{n_l} L_j \rho_j^2 \Delta\xi_j = - \sum_{j=1}^{n_l-1} |\vartheta_{j+1/2}| (\rho_{j+1} - \rho_j)^2 \quad (52)$$

## C Variational formulation and functional minimizer

We aim to calculate the variational (Gateaux) derivative of eq.(25) with respect to  $\vartheta$ , that follows the direction  $h$ :

$$\delta_\vartheta \mathcal{F}[h] \stackrel{\text{def}}{=} \lim_{s \rightarrow 0} \frac{\mathcal{F}(\vartheta + hs) - \mathcal{F}(\vartheta)}{t} \quad (53)$$

Through the classic result of the calculus of variations, the point where  $\mathcal{F}$  is minimized is that which  $\delta_\vartheta \mathcal{F}[h] = 0$  for all possible  $h$  (see also [38]).

Having in mind that by eq.(23) we have  $z^{n+1} = z_{lag}^* - \Delta t \vartheta$  and thus  $\delta_\vartheta z^{n+1} = -\Delta t \times h$ , we calculate term by term the following:

$$\begin{aligned} \delta_\vartheta \mathcal{F}[h] = 2 \iiint_D & \left[ a_\vartheta T_{ref} \vartheta h - a_x \Delta x^2 \frac{\partial}{\partial x} (z^{n+1} - z_{ref}) \frac{\partial h}{\partial x} \right. \\ & \left. - a_\xi \Delta \xi^2 \frac{\partial}{\partial \xi} (z^{n+1} - z_{ref}) \frac{\partial h}{\partial \xi} - a_M \Delta \xi^2 M^2 \frac{\partial z^{n+1}}{\partial \xi} \frac{\partial h}{\partial \xi} \right] dx d\xi \end{aligned} \quad (54)$$

Thus, through integration by parts we conclude that:

$$\begin{aligned} \delta_\vartheta \mathcal{F}[h] = 2 \iiint_D h & \left[ a_\vartheta T_{ref} \vartheta + a_x \Delta x^2 \frac{\partial^2}{\partial x^2} (z^{n+1} - z_{ref}) \right. \\ & \left. + a_\xi \Delta \xi^2 \frac{\partial^2}{\partial \xi^2} (z^{n+1} - z_{ref}) + a_M \Delta \xi^2 \frac{\partial}{\partial \xi} \left( M^2 \frac{\partial z^{n+1}}{\partial x} \right) \right] dx d\xi \end{aligned} \quad (55)$$

$$+ \iint_{\partial D} h \times (\text{boundary terms}) dS \quad (56)$$

substituting the expression  $z^{n+1} = z_{lag}^* - \Delta t \vartheta$  we get that for  $h$  in the interior of  $D$ :

$$\begin{aligned} \delta_\vartheta \mathcal{F}[h] = 2 \Delta t \iiint_D h & \left[ a_\vartheta \frac{T_{ref}}{\Delta t} \vartheta - a_x \Delta x^2 \frac{\partial^2}{\partial x^2} \{ \vartheta - v_{lag} \} \right. \\ & \left. - a_\xi \Delta \xi^2 \frac{\partial^2}{\partial \xi^2} \{ \vartheta - v_{lag} \} - a_M \Delta \xi^2 \frac{\partial}{\partial \xi} \left\{ M^2 \frac{\partial}{\partial \xi} \left( \vartheta - \frac{z_{lag}^*}{\Delta t} \right) \right\} \right] dx d\xi \end{aligned} \quad (57)$$

where  $v_{lag} \stackrel{\text{def}}{=} \frac{z_{lag}^* - z_{ref}}{\Delta t}$ . Since this holds for every  $h$ , we conclude that the minimizer of  $\mathcal{F}$  satisfies eq.(26).